drones

MDPI

Article

Flight Performance Analysis of Industrial-Grade Logistics Slung-Load Unmanned Aerial Vehicles and Research on Flight Operations for Improving Slung-Load System Stability

Wen Zhang [1], Rui Wang [2], Peng Jing [3], Qinsheng Bi [1,*], Yuan Wang [3] and Qing Liu [3]

1 School of Low-Altitude Technology, Jiangsu University, No. 301 Xuefu Road, Zhenjiang 212013, China
2 China Design Group Co., Ltd., No. 9 Ziyun Avenue, Qinhuai District, Nanjing 210014, China
3 School of Automotive and Traffic Engineering, Jiangsu University, No. 301 Xuefu Road, Zhenjiang 212013, China
* Correspondence: qbi@ujs.edu.cn

Highlights

What are the main findings?

- Based on the existing flight control system of industrial-grade logistics drones, quantitatively controlling the drone's suspended load weight, flight mode, speed trajectory, and swing suppression angle can effectively enhance the stability of the suspended load.

What are the implications of the main findings?

- The quantitative analysis examines the effects of load mass, flight mode, speed profile, and swing suppression angle on the suspension stability of industrial-grade logistics drones.
- To improve the stability of suspended loads for industrial-grade logistics drones, a series of actionable flight strategies are proposed.

Abstract

Industrial-grade suspended-load logistics drones have now been widely used in commercial activities. The swing of their suspended loads has always been a major challenge in flight control. At present, most related studies take small quadrotor drones as the research object and employ approaches such as designing novel flight control systems, followed by analysis through theoretical and simulation-based validation. However, research on industrial-grade drones remains lacking, and the results of such studies cannot be quickly applied in engineering practice. Therefore, this paper proposes a set of flight operation guidelines for the existing flight control system of industrial-grade logistics drones. This study conducts flight experiments on commonly used industrial-grade logistics drones to investigate slung-load stability under varying built-in parameters, velocity profiles, and payload weights. The swing parameters are measured and analyzed. The results show that by adjusting relevant parameters, the swing angle and settling time are significantly improved. Finally, based on the experimental analysis results, a set of flight strategies is proposed, which can quickly improve the stability of the slung load of industrial-grade logistics drones using the existing conditions in engineering applications.

Keywords: industrial-grade UAVs; slung load; swing suppression; flight experiment

Check for updates

Academic Editor: Abdessattar Abdelkefi

Received: 15 May 2026
Revised: 27 June 2026
Accepted: 7 July 2026
Published: 15 July 2026

1. Introduction

Industrial-grade logistics UAVs have been increasingly applied to logistics and transportation tasks. Their superiority in transportation is more evident in some complex environments, such as delivering medical supplies to inaccessible areas and transporting tools at construction sites [1–6]. However, current research on UAVs mainly focuses on small quadrotor UAVs, and there is a relative shortage of research on industrial-grade logistics UAVs. This focus does not align with the growing market demand for industrial-grade platforms. In addition, studies on stability mostly concentrate on the development of control algorithms and simulation, largely overlooking the self-adjustment capabilities of UAVs. Research on how the built-in parameters of industrial-grade logistics UAVs and externally adjustable factors like load control the stability of slung loads is still in its infancy. In particular, there is a lack of a set of flight strategies and suggestions that can quickly and conveniently improve the stability of slung loads in engineering applications. This gap motivates the present study.

The research on suppressing the swing of UAV-slung loads is a typical under-actuated, strongly coupled, and non-linear control problem, and the challenges it faces are multi-level and interrelated [7–12]. Based on a comprehensive analysis of the field of suppressing the swing of UAV-slung loads, the key challenges are as follows:

(1) There is strong coupling and under-actuation in the UAV-slung-load system. The UAV has only four independent control inputs, but it needs to stabilize its own six-degree-of-freedom and the two-degree-of-freedom swing of the load. To suppress the swing, the load can only be influenced indirectly and in a coupled manner through the drone.

(2) The strong coupling causes the UAV and the load to interfere with each other, which may damage the stability of the system. Therefore, it is urgent to design an advanced controller based on an accurate geometric or non-linear dynamic model.

(3) In real-world environments, there are numerous factors affecting the stability of slung-load UAVs, making accurate modeling difficult. Moreover, the effectiveness of algorithms highly depends on real-time and precise perception of load swing. However, it is also a major challenge to obtain load information efficiently. Therefore, it is necessary to develop adaptive control and multi-sensor fusion state estimation that do not rely on precise models, enabling the system to adapt to sudden changes online.

(4) It is difficult to unify control performance, computational complexity, and safety robustness. Usually, controllers with high computational complexity have better control performance and safety, but they put great pressure on the platform operation; while simple controllers have poor control performance and safety. Therefore, it is necessary to design an adaptive controller that ensures both safety and high-performance under limited computing power.

To address the second challenge, some scholars have introduced swing dynamics into theories such as under-actuation [13] and non-linear coupling [14,15], but it is still difficult to accurately model and control. A large number of studies have been dedicated to developing advanced control algorithms such as non-linear model predictive control to suppress the swing [16,17].

The design of controllers provides solutions to meet the control requirements and ensure the stability of UAVs [18–23]. Yaşkıran et al. explored the applications of SMC and Fractional-Order Sliding Mode Control (FOSMC) in UAV control systems [24]. By demonstrating the performance advantages and limitations of SMC and FOSMC methods, the literature analysis highlights the current research trends. For example, Bouhabza et al. designed a passivity-based sliding mode controller for quadrotor UAVs by leveraging the robustness of sliding mode control and the energy efficiency based on passivity control theory [25]. The feedback passivation method was used to create a sliding surface with passivity to ensure stability. In addition, a Fractional-Order Reaching Law Sliding Mode (FOSM-ADRC) control method with an Active Disturbance Rejection Controller was proposed [26,27]. This controller combines the Fractional-Order calculus operator and Active Disturbance Rejection Controller (ADRC) technology to enhance the dynamic performance and robustness of the system.

High-accuracy control models have grown, making previous models inadequate [28]. Consequently, scholars have conducted a series of studies focusing on how to improve the accuracy of controllers. A control framework was proposed, which combines Backstepping Sliding Mode Control (BSMC) with a Super-Twisting Observer (STO) [29]. In this scheme, only the position and attitude are directly measured, and the STO reconstructs the linear velocity and angular velocity in real-time. Then, the estimated states are input into the control law, enabling precise trajectory tracking and robust performance without full-state feedback or explicit disturbance compensation. To further improve the control efficiency, a UAV pose control method based on the integration of Active Disturbance Rejection Control (ADRC) and Super-Twisting Sliding Mode Control (ST-SMC) [30] was proposed. This method combines the advantages of ADRC and super-twisting sliding mode algorithms, achieving complementary performance. It not only enhances the system's disturbance-rejection ability and response speed but also effectively alleviates the high-frequency chattering problem often caused by the switching function in traditional sliding mode control.

In addition, geometric control is also one of the most common control methods for rotorcraft UAVs and has been extensively studied. For example, regarding the trajectory-tracking problem of a quadrotor UAV carrying a load, a geometric control method was proposed. The Euler-Lagrange equations are used to model the controlled object. Then, when the load swing angle is close to zero, the model can be linearized [31]. There was also a study that, based on the differential flatness property [28], proposed a non-linear backstepping control scheme and verified the practical performance of the proposed method in experiments. In the above method, the swing of the suspension rope is modeled as an indirect control variable. The movement of the rotary-wing UAV is used to indirectly control the suspension rope, achieving effective swing suppression. However, considering complex application scenarios, the existing control methods still have some shortcomings. In particular, the existing methods have not fully analyzed and addressed the non-linear and state-coupling characteristics of the system. As a result, it is difficult to fully utilize the maneuverability of the rotorcraft UAVs, and it is also difficult to further analyze the overall stability of the system that includes components such as the load, rope, and rotorcraft UAV.

Benefiting from the development of artificial intelligence technology, control technology based on reinforcement learning has made great progress. However, for the attitude control problem of suspended transportation systems, few solutions have been reported in the literature. First, considering the strong-coupling characteristics among the states of the load, rope, and rotary-wing UAV in the system, the existing methods are difficult to apply directly. In particular, due to the curse of dimensionality, widely used discretization methods, including lookup tables [32], Deep Q Network [33,34], etc., are difficult to directly apply to suspended transportation systems. In addition, most of the published reinforcement-learning methods have only been tested in simulations. Considering the widespread model errors, parameter drifts, and external disturbances in practical systems, how to design a reinforcement-learning control strategy that meets the actual task requirements is still full of challenges. At the same time, some researchers have begun to explore application-oriented reinforcement-learning methods, a typical representative of which is the non-linear control method based on intelligent parameters [35]. But so far, most of the literature has only considered systems with fewer states and simple dynamic characteristics. For the flight-control problems of suspended transportation systems, how to design an effective reinforcement-learning strategy still requires in-depth research.

The above-mentioned methods usually require accurate system identification and complex on-board calculations, and thus cannot be applied to all practical scenarios. Moreover, most of these methods take small-scale quadrotor UAVs as the research objects. In contrast, there is still a lack of research on the control of the stability of slung loads regarding the built-in parameters of industrial-grade logistics UAVs and externally adjustable factors such as loads. This also prompts the proposal of flight strategies in this paper to improve the stability of slung loads of industrial-grade UAVs. Specifically, before the start of a flight mission, by identifying the mission type, adjusting the built-in parameters of the UAV, the flight curve, and the load weight, the swing of the slung load can be suppressed.

Based on the above analysis, this paper proposes a flight-control scheme suitable for improving the stability of slung loads of industrial-grade logistics UAVs. The main research contributions are as follows:

(1) Experimental Dataset: A comprehensive outdoor flight dataset is constructed for the first time for an industrial-grade slung-load unmanned aerial vehicle (DJI FlyCart 30) under varying payload weights, flight modes, velocity profiles, and swing suppression angles.
(2) Quantitative Findings: The trade-off among payload weight, swing amplitude, and settling time is identified. It is discovered that the slung-load swing angle first decreases and then increases as the swing suppression angle increases. In addition, the effects of velocity planning are clarified.
(3) Practical Guidelines: Optimization recommendations are provided for payload selection, velocity planning, and parameter tuning to enhance the flight stability of the UAV.

In order to obtain flight operation guidelines for improving the load-carrying stability of industrial-grade logistics UAVs, this paper conducts outdoor simulation tests of UAV logistics distribution and carries out detailed data analysis. The test results show that current industrial-grade logistics UAVs already possess good stability, but there are still issues such as insufficient endurance and unstable speed changes. In addition, through test analysis, it is found that setting different load masses, speed curves, load-carrying modes, and anti-swing angles can quickly and effectively improve load-carrying stability, and a set of flight operation guidelines has been formed. Through comparison, it is found that in this study, the reduction degree of the swing-angle amplitude is close to that of research on accurate modeling and controller design. In terms of swing-angle elimination control, the reduction range of the swing-angle amplitude even exceeds that of some new-model research and controller-design research.

The remaining part of this paper is structured as follows. In Section 2, the dynamics of the UAV slung-load system are analyzed, reasonable model assumptions are established, and the dynamic equations of the system are derived using the Euler-Lagrange method. Section 3 elaborates in detail on the experimental platform and experimental scheme design of this study, and also explains the data-processing procedure. Section 4 presents the experimental results, analyzes the experimental data, and proposes corresponding strategies to improve the flight stability of the UAV. Section 5 conducts a discussion. Section 6 summarizes this paper and proposes future research directions.

2. Dynamic Model Analysis of the Suspension System

2.1. Model Assumptions and Definition of Coordinate System

2.1.1. Model Assumptions

To ensure the simplicity and analyticity of the model, appropriate assumptions are made for the system according to the actual flight conditions:

(1) The structure of the quadrotor airframe is rigid, and its center of mass remains fixed. The airframe has a symmetrical structure, and the moments of inertia about each axis, calculated with respect to the center of mass, are I_x, I_y, and I_z respectively (assuming that the principal axis system coincides with the body axis system, and the products of inertia are zero).

(2) The load suspension point is located at the center of mass of the aircraft and coincides with the origin of the body coordinate system. That is, the line of tension acts through the center of mass and does not generate additional torque on the aircraft.

(3) The volume of the load is negligible compared to the rope length, and it can be regarded as a mass point. Also, during the flight, the load always moves below the aircraft, meaning that θ_x and θ_y are always within the range of $[-2\pi, 2\pi]$ (to prevent the load from hanging upside-down above the aircraft).

(4) The mass of the suspension cable connecting the aircraft and the load is negligible; it is inextensible and always taut. In other words, the rope only transmits tension, without considering bending and elastic deformation, and the rope length is a constant.

The above assumptions ensure that the model is simple and captures the main dynamic characteristics. On this basis, a dynamic model of the single-pendulum suspension system is established.

2.1.2. Coordinate System Definition

In the modeling of a quadrotor with a slung load, it is first necessary to define the coordinate systems involved: the inertial frame $I\{X_I, Y_I, Z_I\}$, the quadrotor body frame $B\{x, y, z\}$, and the load body frame $B_p\{x_p, y_p, z_p\}$, as illustrated in Figure 1. The inertial frame $I\{X_I, Y_I, Z_I\}$ is defined as a North-East-Down (NED) coordinate system, which describes the absolute position of the quadrotor in space, with X_I pointing north, Y_I pointing east, and Z_I pointing vertically downward toward the ground. The quadrotor body frame $B\{x, y, z\}$ has its origin coincident with the quadrotor's center of mass, with x pointing forward along the nose direction, y pointing to the right side of the fuselage, and z perpendicular to both x and y, pointing downward. The load body frame $B_p\{x_p, y_p, z_p\}$ has its origin at the load's center of mass, with x_p pointing forward, y_p pointing to the right, and z_p directed along the suspension cable toward the load.

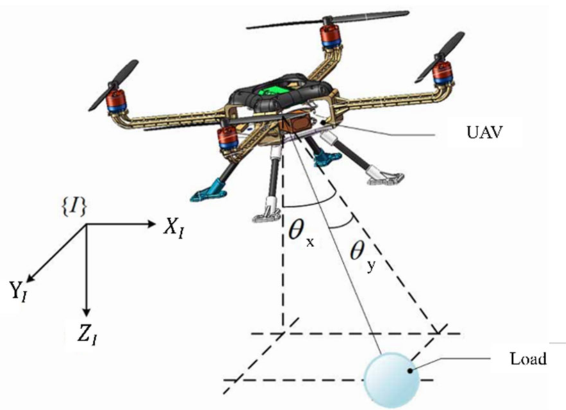

Figure 1. Quadrotor suspended load system.

2.2. Model Assumptions: Establishing the Single-Pendulum Suspension Dynamics Model Based on the Euler-Lagrange Method

As shown in Figure 1, the single-pendulum suspension system refers to the configuration where a UAV suspends a load through a flexible rope. Based on the aforementioned assumptions, the system consists of the following components: the UAV (with mass M), the suspension rope (with length l and negligible mass), and the load modeled as a point mass (with mass m). The system has a total of n = 6 + 2 = 8 degrees of freedom, including:

(1) Three translational degrees of freedom of the UAV (positions along the axes);
(2) Three rotational degrees of freedom of the UAV (Euler angles about the body-fixed axes X_b, Y_b, Z_b);
(3) Two swing degrees of freedom of the load (swing angles θ_x, θ_y).

The following generalized coordinates are selected to describe the system state:

$$q = \left[x, y, z, \varnothing, \theta, \psi, \theta_x, \theta_y\right]^T \tag{1}$$

According to the geometric analysis, the following relationships hold (the subscript "p" represents "payload") [36]:

$$\xi_p = \xi + Pl \tag{2}$$

where $\xi_p = \left(x_p, y_p, z_p\right)$ is the position of the payload in the inertial coordinate system, and l is the length of the pendulum line.

$$P = Rot(\theta_x)Rot\left(\theta_y\right) = \begin{bmatrix} C_y & S_xS_y & S_yC_x \\ 0 & C_x & -S_x \\ -S_y & S_xC_y & C_xC_y \end{bmatrix} \tag{3}$$

where $Rot(\theta_x)$ and $Rot(\theta_y)$ are the rotation matrices about the axes Y_h and X_h in the coordinate system h, S_x, S_y are $sin\theta_x$, $sin\theta_y$, and C_x, C_y are $cos\theta_x$, $cos\theta_y$. These formulas give the position of the payload in the inertial system. The offset vector of the payload relative to the aircraft can be expressed as follows:

$$r_p = \left(x_p - x, y_p - y, z_p - z\right) \tag{4}$$

Taking the derivative of Equation (2) with respect to time, the relationship between the aircraft velocity and the rate of change in the pendulum angle can be obtained

$$\begin{aligned} \dot{x}_p &= \dot{x} - l\left(\dot{\theta}_x S_x S_y - \dot{\theta}_y C_x C_y\right) \\ \dot{y}_p &= \dot{y} - l\dot{\theta}_x C_x \\ \dot{z}_p &= \dot{z} - l\left(\dot{\theta}_x S_x C_y + \dot{\theta}_y C_x S_y\right) \end{aligned} \tag{5}$$

Define the velocities of the load mass point and the center of mass of the aircraft as follows:

$$\boldsymbol{V}_p = \left(\dot{x}_p, \dot{y}_p, \dot{z}_p\right),\ \boldsymbol{V}_u = \left(\dot{x}, \dot{y}, \dot{z}\right) \tag{6}$$

The rotational motion of the quadrotor is described by the relationship between the rate of change in Euler angles and the angular velocity vector. Let $\omega = [p, q, r]^T$ be the components of the angular velocity vector in the body coordinate system. The relationship between the derivatives of Euler angles and the angular velocity is as follows [37,38]:

$$\begin{bmatrix} p \\ q \\ r \end{bmatrix} = \begin{bmatrix} 1 & 0 & -sin\theta \\ 0 & cos\varnothing & cos\theta sin\varnothing \\ 0 & -sin\theta & cos\theta cos\varnothing \end{bmatrix} \begin{bmatrix} \dot{\varnothing} \\ \dot{\theta} \\ \dot{\psi} \end{bmatrix} \tag{7}$$

This Jacobian matrix is derived from the standard Euler-angle kinematics and will be used later to express the rotational kinetic energy of the aircraft.

Based on the above selection of generalized coordinates, calculate the total kinetic energy T and total potential energy V of the system. They each include two parts: the aircraft and the load.

The kinetic energy of the aircraft T_u includes two parts: translational and rotational [36]

$$T_u = \frac{1}{2}M\left(\dot{x}^2 + \dot{y}^2 + \dot{z}^2\right) + \frac{1}{2}\left(I_x P^2 + I_y q^2 + I_z r^2\right) \tag{8}$$

where p, q, r can be expressed in terms of φ, θ, ψ using Equation (8). If the inertia tensor of the aircraft is assumed to be a diagonal matrix and there are no gyroscopic coupling terms (i.e., $I_{xy} = I_{yz} = I_{zx} = 0$), then it can be approximated as follows:

$$T_u \approx \frac{1}{2}M(\dot{x}^2 + \dot{y}^2 + \dot{z}^2) + \frac{1}{2}(I_x\dot{\varnothing}^2 + I_y\dot{\theta}^2 + I_z\dot{\psi}^2) \tag{9}$$

If the load is regarded as a mass point, its kinetic energy T_p is [36]

$$T_p = \frac{1}{2}m\left(\dot{x}_p{}^2 + \dot{y}_p{}^2 + \dot{z}_p{}^2\right) \tag{10}$$

where $\dot{x}_p$, $\dot{y}_p$, $\dot{z}_p$ are given by Equation (2). This expression contains the translational velocity of the aircraft, the derivatives of the pendulum angles, and the coupling terms between them.

Therefore, the total kinetic energy of the system is

$$T = T_u + T_p \tag{11}$$

The total potential energy of the system is caused by gravity. Assume that the direction of the z-axis of the inertial system is downward, and the ground is set as the zero-potential surface; then [36]

$$V = -Mgz - mgz_p \tag{12}$$

By substituting $z_p = z - lc_x c_y$ into it, we get

$$V = -Mgz - mg\left(z + lC_x C_y\right) = -(M+m)gz - mglC_x C_y \tag{13}$$

Then, according to the Euler–Lagrange method, define the Lagrangian

$$L = T - V = T_u + T_p - V \tag{14}$$

And by combining (8), (10), and (11), the Lagrangian can be expressed as:

$$\begin{aligned} L(q,\dot{q}) = {} & \tfrac{1}{2}(M+m)\left(\dot{x}^2 + \dot{y}^2 + \dot{z}^2\right) + \tfrac{1}{2}\left(I_{xx}S_\theta{}^2 + I_{yy}C_\theta{}^2 S_\varnothing{}^2 + I_{zz}C_\theta{}^2 C_\varnothing{}^2\right)\dot{\psi}^2 \\ & + \tfrac{1}{2}\left(I_{yy}C_\varnothing{}^2 + I_{zz}S_\varnothing{}^2\right)\dot{\theta}^2 + \tfrac{1}{2}I_{xx}\dot{\varnothing}^2 + \tfrac{1}{2}ml^2 C_x{}^2\dot{\theta}_y{}^2 \\ & + \tfrac{1}{2}ml^2\dot{\theta}_x{}^2 - I_{xx}s_\theta\dot{\psi}\dot{\varnothing} + (I_{yy} - I_{zz})c_\theta c_\varnothing s_\varnothing\dot{\psi}\dot{\theta} \\ & + ml\dot{\theta}_y\left(C_y C_x\dot{x} - S_y C_x\dot{z}\right) - ml\dot{\theta}_x\left(S_x S_y\dot{x} + C_x\dot{y} + S_x C_y\dot{z}\right) + Mgz \\ & + mg\left(z + lC_x C_y\right) \end{aligned} \tag{15}$$

Based on the Lagrange equation [39], the relationship between the Lagrangian of the system and the system states is derived as follows:

$$\frac{d}{d_t}\left(\frac{\partial L}{\partial \dot{q}_i}\right) - \frac{\partial L}{\partial q_i} = BU \tag{16}$$

where U is the control input of the system $U = \begin{bmatrix} F & \tau_{\varnothing} & \tau_\theta\ \tau_\psi \end{bmatrix}^T$, and corresponding dynamic equations are established for each generalized coordinate. Next, according to the definition of the system state $q = \left[x, y, z, \varnothing, \theta, \psi, \theta_x, \theta_y\right]^T$, the Lagrangian is derived term by term, and the main forms of the motion equations of the system in each direction and their physical meanings are given respectively.

Translational x-direction

$$\frac{d}{d_t}\left(\frac{\partial L}{\partial \dot{x}}\right) - \frac{\partial L}{\partial x} = F_x \tag{17}$$

Since x in L only appears in the kinetic energy (through $\dot{x}$ and $\dot{x}_p$) and the potential energy of the load (through x_p), the derivation gives

$$\begin{gathered} F_x = (M+m)\ddot{x} - mlS_xS_y\ddot{\theta}_x + mlC_xC_y\ddot{\theta}_y - 2mlS_xC_y\dot{\theta}_x\dot{\theta}_y \\ -mlC_xS_y\dot{\theta}_x^{\ 2} - mlC_xS_y\dot{\theta}_y^{\ 2} \end{gathered} \tag{18}$$

This equation describes the motion along the inertial x-axis. $(M+m)\ddot{x}$ is the inertial force of the aircraft-load system as a whole, and the subsequent terms come from the traction effect of the load's swing on the aircraft (the component of the rope tension in the x-direction). It can be seen that when the load is stationary (θ_x, θ_y) and $F_x = 0$, the above equation simplifies to $(M+m)\ddot{x} = 0$, that is, the center of mass of the system moves in a straight line at a constant speed without external force. When the aircraft accelerates or the load swings, the two generate a coupled force that affects $\ddot{x}$.

By the same token, for the translational y-direction

$$\frac{d}{d_t}\left(\frac{\partial L}{\partial \dot{y}}\right) - \frac{\partial L}{\partial y} = (M+m)\ddot{y} - mlC_x\ddot{\theta}_x + mlS_x\dot{\theta}_x^{\ 2} \tag{19}$$

This equation describes the motion law of the system in the y-axis direction of the inertial coordinate system. Since $y_p = y - ls_y$ is set during the modeling, it can be seen that the change in the pendulum angle θ_y will directly affect the position of the load in the y-direction, and thus will also exert a certain pulling force on the aircraft. In the above formula, the $\ddot{\theta}_y$ term reflects the traction force caused by the lateral swing acceleration of the load, and the other terms reflect the coupling between the aircraft's motion and the load's swing.

Translational z-direction

$$\begin{gathered} \tfrac{d}{d_t}\left(\tfrac{\partial L}{\partial \dot{z}}\right) - \tfrac{\partial L}{\partial z} = (M+m)\ddot{z} - mlS_xC_y\ddot{\theta}_x - mlC_xS_y\ddot{\theta}_y + 2mlS_yS_x\dot{\theta}_x\dot{\theta}_y \\ -mlC_yC_x\dot{\theta}_x^{\ 2} - mlC_yC_x\dot{\theta}_y^{\ 2} + (M+m)g \end{gathered} \tag{20}$$

This equation is the dynamic equilibrium equation in the vertical direction. The first six terms on the left-hand side are the vertical inertial forces of the aircraft-load system as a whole and the coupling force terms generated by the load's swing. $(M+m)g$ is the total gravity of the system. When the system is in a stable hovering state, $\varnothing \approx 0$, $\theta \approx 0$ and $\dot{\theta}_x \approx 0$, $\dot{\theta}_y \approx 0$. At this time, the above equation simplifies to

$$F = (M+m)g \tag{21}$$

That is, the thrust is equal to the total gravity of the system to achieve balance. When the system is tilted or the load swings, the thrust not only has to bear the gravity but also resist the disturbance terms brought by the load, that is, the acceleration-related terms such as θ_x, θ_y in the formula.

Rotational φ (roll) and θ (pitch) directions

$$\tau_{\varnothing} = I_{xx}\ddot{\varnothing} - I_{xx}S_{\theta}\ddot{\psi} - I_{xx}\dot{\psi}\dot{\theta}C_{\theta} - \left(I_{yy} - I_{zz}\right)\left(S_{\varnothing}C_{\varnothing}C_{\theta}{}^{2}\dot{\psi}^{2} - \dot{\theta}^{2}S_{\varnothing}C_{\varnothing} + \dot{\psi}\dot{\theta}\, C_{\theta}C_{2\varnothing}\right) \tag{22}$$

$$\begin{aligned}\tau_{\theta} = &\left(I_{yy}C_{\varnothing}{}^{2} + I_{zz}S_{\varnothing}{}^{2}\right)\ddot{\theta} + \left(I_{yy} - I_{zz}\right)C_{\theta}C_{\varnothing}S_{\varnothing}\ddot{\psi} \\ &+\left\{I_{xx}\dot{\psi}C_{\theta} + \left(I_{yy} - I_{zz}\right)\left(-2\dot{\theta}S_{\varnothing}C_{\varnothing} + \dot{\psi}C_{\theta}C_{\varnothing}{}^{2} - \dot{\psi}C_{\theta}S_{\varnothing}{}^{2}\right)\right\}\dot{\varnothing} \\ &+S_{\theta}C_{\theta}\left(-I_{xx} + I_{yy}S_{\varnothing}{}^{2} + I_{zz}C_{\varnothing}{}^{2}\right)\dot{\psi}^{2}\end{aligned} \tag{23}$$

Rotational ψ-direction (yaw)

$$\begin{aligned}\tau_{\psi} = &-I_{xx}S_{\varnothing}\ddot{\varnothing} + \left(I_{yy} - I_{zz}\right)C_{\theta}C_{\varnothing}S_{\varnothing}\ddot{\theta} + \left\{I_{xx}S_{\theta}{}^{2} + C_{\theta}{}^{2}\left(I_{zz}C_{\varnothing}{}^{2} + I_{yy}S_{\varnothing}{}^{2}\right)\right\}\ddot{\psi} \\ &+\left(I_{yy} - I_{zz}\right)\dot{\varnothing}C_{\theta}{}^{2}S_{\varnothing}C_{\varnothing}\dot{\psi} - \left\{I_{xx}\dot{\theta}C_{\theta} - \left(I_{yy} - I_{zz}\right)\dot{\psi}C_{\theta}{}^{2}C_{\varnothing}S_{\varnothing}\right\}\dot{\varnothing} \\ &+\left\{I_{xx}\dot{\psi}S_{\theta}C_{\theta} - \left(I_{yy} - I_{zz}\right)\left(\dot{\theta}S_{\theta}C_{\varnothing}S_{\varnothing} + \dot{\varnothing}C_{\theta}S_{\varnothing}{}^{2} - \dot{\varnothing}C_{\theta}C_{\varnothing}{}^{2}\right)\right\}\dot{\theta} \\ &+\left\{I_{xx}\dot{\theta}S_{\theta}C_{\theta} - 2\left(I_{yy}S_{\varnothing}{}^{2} + I_{zz}C_{\varnothing}{}^{2}\right)\dot{\theta}S_{\theta}C_{\theta}\right\}\dot{\psi}\end{aligned} \tag{24}$$

The terms related to the pendulum angles θ_x, θ_y of the load are not explicitly included in these equations. This is because in the modeling, it is assumed that the suspension point of the rope is located at the center of mass of the aircraft, and the rope tension does not generate additional torque on the aircraft. Therefore, the load swing does not directly affect the rotational dynamics of the airframe. The change in the aircraft's attitude is mainly affected by its own moment of inertia and control torque.

Load swing θ_x, θ_y equations

$$\left(I_p + ml^2\right)\ddot{\theta}_x - mlS_xS_y\ddot{x} - mlC_x\ddot{y} - mlC_yS_x\ddot{z} + ml^2S_xC_x\dot{\theta}_y{}^{2} + mlgS_yC_y = 0 \tag{25}$$

$$\left(I_p + ml^2C_x{}^2\right)\ddot{\theta}_y - 2ml^2S_xC_x\dot{\theta}_x\dot{\theta}_y + mlC_xC_y\ddot{x} - mlS_yC_x\ddot{z} + mlgS_yC_x = 0 \tag{26}$$

Equations (25) and (26) describe the motion of the load. It can be seen that there is a coupling relationship between the pendulum angles θ_x, θ_y and the three-axis translation of the fuselage. If θ_x, θ_y are extracted to the right-hand side of the equation, the equation can be expressed as $f_x = (\ddot{x}, \ddot{z})$, $f_y = (\ddot{x}, \ddot{y}, \ddot{z})$, where $f_x(\cdot)$, $f_y(\cdot)$ express the non-linear relationship between $\ddot{\theta}_x$, $\ddot{\theta}_y$ and $\ddot{x}, \ddot{y}, \ddot{z}$. And it can be seen from the above formula that, under the model assumptions in Section 2.1, there is no dynamic coupling between the load pendulum angle and the fuselage attitude.

Equations (18)–(26) together form the dynamic model of the single-pendulum hanging system. They completely describe the dynamic behavior of the system: the translation of the aircraft is restricted by the load swing, the load swing is excited by the aircraft's movement, and the attitude of the aircraft affects the translation through the thrust direction but is not directly twisted by the load. This set of equations is a highly non-linear coupled system.

It should be emphasized that the simplified model described above is not intended for controller design or parameter identification; rather, it serves solely as a theoretical tool to explain the experimental phenomena observed in Section 4.

3. Materials and Methods

3.1. Experimental Platform

3.1.1. UAV

The UAV used in this experiment is the DJI FlyCart30 as shown in Figure 2. The FC30 adopts a 4-axis, 8-propeller multi-rotor configuration, sourced by DJI, from Shenzhen, China. In the dual-battery mode, it has a maximum load capacity of 30 kg and a maximum full-load flight range of 16 km. The whole machine has an IP55 protection level, can adapt to an operating environment temperature from −20 °C to 45 °C, and has a maximum flight altitude of 6000 m. It has strong environmental adaptability and can be applied to all-weather, wide-temperature, and cross-altitude operation scenarios. This model adopts the aerial suspension load mode, which supports functions such as intelligent swing elimination and emergency fusing.

Figure 2. DJI FlyCart30.

The flight control platform realizes task automation control through the DJI Pilot 2 application and the DJI SDK. The UAV is equipped with the standard FC30 flight control. For different environments, the UAV can adjust two flight modes: the suspension load mode and the normal mode. In the suspension load mode, the UAV can only be manually operated, with a maximum speed of 3 m/s. The normal mode is a commonly used flight mode for UAV delivery. By setting the route in advance, the UAV can achieve automatic flight.

3.1.2. Pendulum Angle Measurement System

A crucial aspect of this study is the accurate measurement of load swing. A custom-simulated transportation load system was constructed. An independent IMU module was firmly installed within the system to measure its attitude at a frequency of 1 Hz. The IMU data was transmitted to the pan-tilt head via a 4G wireless network and recorded for post-processing. The load was suspended 5 m below the center of gravity of the drone using a taut nylon rope.

Based on the Lagrangian equation and simple pendulum theory, for a rope length of 5 m, the period T of the simple pendulum is approximately 4.48 s, with a corresponding natural frequency f_n of about 0.22 Hz. According to the Nyquist sampling theorem, the sampling frequency must be greater than $2f_n$ (0.44 Hz). The sampling frequency of the IMU adopted in this study is 1 Hz, which meets the requirement and is sufficient to capture the dominant frequency component of the pendulum swing.

SINDT-LTE is a high-performance three-dimensional motion attitude measurement system based on MEMS technology. It contains motion sensors such as a three-axis gyroscope and a three-axis accelerometer. By integrating various high-performance sensors and an attitude dynamics algorithm engine, and combining with a high-dynamic Kalman filter fusion algorithm, it can provide high-precision, high-dynamic, and real-time compensated three-axis attitude angles.

As shown in Figure 3, the axes of the sensor are marked on it. The direction to the right is the x-axis, the upward direction is the y-axis, and the axis perpendicular to the plane is the z-axis. The angle of the x-axis refers to the inclination angle of rotation around the x-axis, the angle of the y-axis refers to the inclination angle of rotation around the y-axis, and the angle of the z-axis refers to the heading angle.

Figure 3. IMU Attitude Measurement System.

3.1.3. Data Acquisition and Processing System

To accurately obtain the load pendulum angle information of the UAV hanging system, the data acquisition and processing system shown in Figure 4 was set up in this experiment. The system consists of an Inertial Measurement Unit (IMU), a4G wireless transmission module, and a ground station, enabling the synchronous recording and analysis of the flight state and load swing.

(1) System Framework Diagram

The following Figure shows the connection relationships and data flow among various hardware modules:

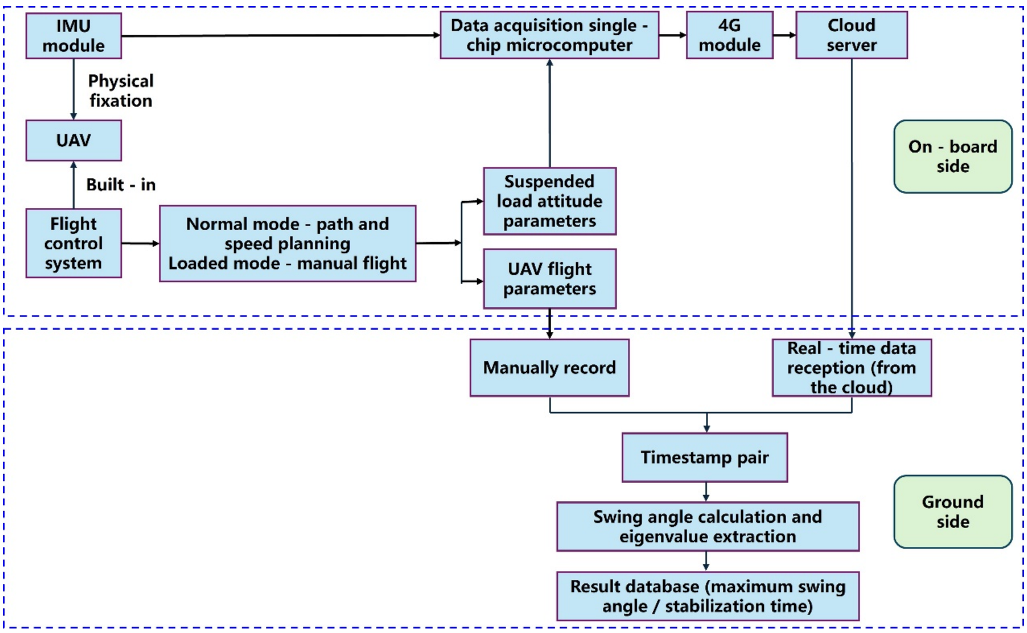

Figure 4. Block diagram of the data acquisition and processing system.

On the airborne side, the IMU is directly fixed near the center of mass of the load. It samples the three-axis acceleration and angular velocity at a sampling rate of 1 Hz. The internal Digital Signal Processor (DSP) runs a Kalman filter in real-time to output stable Euler angles (roll angle, pitch angle, yaw angle). The data acquisition unit adds a time stamp from GPS timing to the Euler angles and sends them to the ground station at a frequency of 1 Hz through the 4G module. The ground station receives the data stream from the 4G module via the cloud server and pushes it to the ground-station software. The time when the UAV reaches each waypoint in the route is manually recorded. In the ground station, the time-stamp alignment module fuses the IMU data and the manually recorded logs along a unified time axis. Subsequently, the synthetic pendulum angle of the load is calculated, and the maximum pendulum angle and the stabilization time are extracted.

(2) Data Processing Flow

The raw IMU data is processed by the internal Kalman filter to output Euler angles, and the subsequent processing is completed by the ground-station software. The specific process is shown in Figure 5.

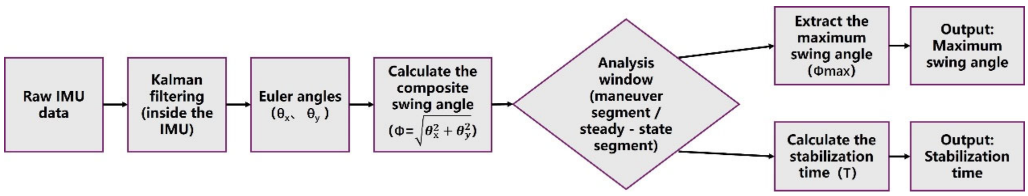

Figure 5. IMU data processing flow.

The detailed processes of each step are as follows:

The IMU sensor has an integrated 9-axis fusion algorithm. It uses the Kalman filter to suppress vibration noise and gyro drift, and outputs smooth, drift-free absolute Euler angles. This step performs real-time noise reduction and attitude calculation on the raw data, eliminating the need for additional processing by the user;

The filtered Euler angles are output through a serial port or SPI bus. In this experiment, the IMU used outputs the roll, pitch, and yaw angles at a frequency of 1 Hz, with a unit of 0.01°.

Since the load is a mass point suspended below the UAV, its absolute pendulum angle is not a single Euler angle component, but the total angle by which the rope deviates from the vertical direction. According to the coordinate system rotation relationship, the synthetic pendulum angle Φ is calculated by the following formula:

$$\Phi = \sqrt{\theta^2 + \varphi^2} \tag{27}$$

where θ is the pitch angle of the load, and φ is the roll angle. This formula combines the tilts in two orthogonal directions into an equivalent pendulum angle, and its physical meaning is the angle between the rope and the direction of gravity. When the load swings only in one plane (such as the front-back direction), $\theta \approx 0$, then $\Phi = | \varphi |$.

The maximum pendulum angle Φ_{max} is the global maximum value of the synthetic pendulum angle $\Phi(t)$ within a 10 s time window after the UAV completes acceleration-deceleration maneuvers (such as changing from a constant-speed flight to hovering). This indicator reflects the peak value of the transient response. The stabilization time t_s refers to the minimum time required for the pendulum angle to enter and remain within the threshold of $\pm 2^\circ$ without exceeding it again.

Stabilization time T_s is defined as the minimum time required for the swing angle to enter and remain within the threshold of $\pm 2^\circ$ without exceeding it again. Calculation method: Starting from the end time T_0 of the maneuver, find the last moment T_{last} that satisfies $|\Phi(t)| > 2°$, then $T_s = T_{last} - T_0$. If it still does not stabilize within 20 s, it is recorded as ">20 s".

3.2. Experimental Design

Four independent experiments were conducted to isolate the effects of different factors on load stability. All experiments were repeated five times to ensure the accuracy of statistical data. Boundary conditions of each group of experiments are presented in Table 1.

Table 1. Boundary conditions of each group of experiments.

Experiment	Grouping	Suspended Load Mass	Flight Mode	Flight Route	Pendulum-Damping Angle
Experiment 1	Group 1	6 kg	Normal mode	Trapezoidal velocity curve	10°
	Group 2	15 kg			
Experiment 2	Group 1	15 kg	Suspended load mode	Trapezoidal velocity curve	10°
	Group 2		Normal mode		
Experiment 3	Group 1	15 kg	Normal mode	S-shaped velocity curve,	10°
	Group 2			trapezoidal velocity curve	
Experiment 4	Group 1	15 kg	Normal mode	Trapezoidal velocity curve	10°
	Group 2				30°
	Group 3				50°

(1) Experiment 1

Comparison of Suspended Loads: A 330 m straight-line path was planned for the UAV using the ground station. The maximum load-carrying capacity of the UAV used in this experiment is 30 kg. Taking both flight range and safety into account, Experiment 1 was divided into two groups. The masses of each group were 6 kg and 15 kg respectively, corresponding to the low-load and medium-load transportation states of the UAV.

(2) Experiment 2

Comparison of Flight Modes: A 130 m straight-line path was planned for the UAV using the ground station. The experiment was set up in two groups. One group flew in the normal mode, and the other group flew in the load-carrying mode. The attitudes of the suspended load in the two flight modes were recorded respectively.

(3) Experiment 3

Comparison of Speed Trajectories: The UAV flew along a 600 m path in the normal mode using two different speed curves: Trapezoidal Curve and S-Curve. The trapezoidal curve is a curve with rapid speed changes. The UAV accelerates rapidly to 10 m/s, flies at a constant speed, and then decelerates rapidly to zero. The S-shaped curve is a curve with slow speed changes. After the UAV takes off, its speed increases by 2 m/s every 60 m. After the speed reaches 10 m/s, it decelerates slowly to 0 m/s.

(4) Experiment 4

Comparison of Anti-swing Parameters: A 600 m flight route was set. The trapezoidal speed curve was adopted, and the UAV was set to the normal flight mode. The anti-swing angles of the UAV were adjusted to 10°, 30°, and 50° in sequence, and the flight was carried out in three groups.

4. Results

In this section, the flight data of the UAV under various conditions are analyzed. After confirming the sufficient reliability of each dataset, statistical tests are performed to examine inter-group differences attributable to the experimental factors, and the observed phenomena are discussed. The analytical results indicate that by adjusting the above parameters, the swing angle of the slung load can be effectively reduced, thereby improving the stability of the load.

4.1. Data Stability Analysis

In this subsection, based on the flight data from four sets of experiments, a statistical analysis is conducted on the peak swing angles of the UAV slung-load system under varying payload masses, flight modes, velocity profiles, and swing suppression angles. Each experimental condition was repeated in multiple independent flights, and incomplete data sets were excluded. The peak swing angle (in degrees) of the load was extracted from each flight as the analysis indicator. First, the intra-group stability of all experimental data is systematically evaluated, followed by statistical tests on inter-group differences under the influence of each factor. The significance level for all statistical analyses is set at $\alpha = 0.05$.

4.1.1. Intra-Group Variability Analysis

The purpose of the data stability analysis is to verify whether the peak swing angles obtained from repeated flights under each experimental condition exhibit good consistency, thereby ensuring the reliability of subsequent inter-group comparisons. Since the number of replicates per group is relatively small (n = 3 or n = 5) after excluding invalid data, the assumption of normality for large samples is not satisfied. Therefore, the coefficient of variation (CV) is primarily adopted as the quantitative indicator of intra-group consistency. In addition, the mean, standard deviation, minimum, maximum, and range are reported for each group to provide a comprehensive view of the data distribution.

Generally, it is considered that CV < 10% indicates excellent repeatability; 10% $\leq$ CV < 20% indicates good repeatability and is acceptable; 20% $\leq$ CV < 30% indicates a certain degree of dispersion but remains acceptable in engineering experiments; and CV $\geq$ 30% indicates considerable data variability, requiring cautious interpretation or investigation of anomalous causes. For groups with only three replicates, the CV is used as a reference only, and the range along with the raw data are also considered for comprehensive judgment.

(1) Data Stability under Different Payload Masses

Experiment 1 includes two payload conditions, 6 kg and 15 kg, with the flight mode, velocity profile, and swing suppression angle kept consistent. The peak swing angle data and descriptive statistics for the two conditions are presented in Table 2.

Table 2. Descriptive statistics of peak swing angle for each group in Experiment 1.

Payload Mass (kg)	n	Peak Swing Angle (°)	Mean (°)	Standard Deviation (°)	Min (°)	Max (°)	Range (°)	CV (%)
6	5	14.51, 29.03, 25.61, 35.71, 29.20	26.81	7.49	14.51	35.71	21.2	27.9
15	3	21.17, 25.96, 20.53	22.55	2.91	20.53	25.96	5.43	12.9

For the 6 kg payload group, the mean peak swing angle across five flights was 26.81°, with a standard deviation of 7.49° and a coefficient of variation (CV) of 27.9%. An examination of the raw data reveals that, apart from the first flight (14.51°), which was notably lower than the others, the remaining four readings ranged from 25° to 36°. Specifically, the range of this group reached 21.20°, making it one of the largest ranges observed across all experiments, indicating that the 6 kg payload was considerably affected by external disturbances (e.g., airflow variations, control deviations) across different flight runs. The highest value (35.71°) was recorded in the fourth flight, whereas the lowest value (14.51°) occurred in the first flight, resulting in a difference of 21.20° between the two.

It should be noted that the relatively light 6 kg payload is more susceptible to random perturbations such as gusts under identical external excitations, and its swing response exhibits higher sensitivity to initial conditions and environmental variations. This is considered the physical cause of the greater dispersion observed in this group, rather than being attributable to measurement errors. No equipment anomalies or operational errors were recorded during any of the five flights; therefore, all data points were retained.

For the 15 kg payload group, the mean peak swing angle across three flights was 22.55°, with a standard deviation of 2.91° and a CV of 12.9%. Although the sample size is relatively small (n = 3), the available data, 21.17°, 25.96°, and 20.53°, show a range of 5.43°, which is substantially smaller than the 21.20° observed in the 6 kg group, indicating significantly better repeatability of the swing response under the 15 kg condition. Compared with the 6 kg group, the CV of the 15 kg group decreased by approximately 15 percentage points (from 27.9% to 12.9%), suggesting that a heavier payload possesses greater inertia and enhanced resistance to external disturbances, thereby yielding higher consistency across repeated flights.

In summary, the data stability of the 15 kg group (CV = 12.9%) is markedly superior to that of the 6 kg group (CV = 27.9%), demonstrating that increasing the payload mass contributes to improved repeatability in experimental trials. Although the 6 kg group exhibits considerable variability, the underlying physical causes are well understood, and no outliers warranting exclusion are present. Consequently, both datasets are considered suitable for subsequent inter-group comparative analyses.

(2) Data Stability under Different Flight Modes

Experiment 2 compared the effects of two flight modes, normal mode and slung-load mode, on the load swing angle. Both modes were configured with a 15 kg payload, a trapezoidal velocity profile, and a swing suppression angle of 10°. The peak swing angle data and descriptive statistics for the two modes are presented in Table 3.

Table 3. Descriptive statistics of peak swing angle for each group in Experiment 2.

Flight Mode	n	Peak Swing Angle (°)	Mean (°)	Standard Deviation (°)	Min (°)	Max (°)	Range (°)	CV (%)
Normal mode	5	7.49, 8.71, 14.14, 13.15, 13.10	11.32	3.00	7.49	14.14	6.65	26.5
Slung-load mode	5	7.96, 17.49, 10.06, 12.22, 13.33		12.21	3.66	7.96	17.49	9.53

For the normal mode (autonomous waypoint flight), the mean peak swing angle across five flights was 11.32°, with a standard deviation of 3.00° and a coefficient of variation (CV) of 26.5%. An examination of the raw data reveals a certain degree of bifurcation among the five results: the first two flights (7.49° and 8.71°) yielded relatively small swing angles, whereas the latter three flights (14.14°, 13.15°, and 13.10°) exhibited notably larger angles with a much narrower range of only 1.04°. The overall range for this group was 6.65°. This bifurcation may be attributed to variations in wind speed or waypoint tracking accuracy across different flight runs. Nevertheless, no extreme outliers were observed in this group.

For the slung-load mode (manual remote-controlled flight), the mean peak swing angle across five flights was 12.21°, with a standard deviation of 3.66° and a CV of 30.0%. The raw data show that the second flight (17.49°) was markedly higher than the other four, representing the maximum of the group, while the first flight (7.96°) was the minimum, yielding a difference of 9.53° between the two. When the second flight was excluded, the mean of the remaining four flights was 10.89°, with a standard deviation of 2.46° and a CV of approximately 22.6%, indicating a considerable reduction in dispersion. This suggests that the randomness inherent in manual control operations—such as variations in joystick deflection—may be one of the primary contributors to data fluctuation in the slung-load mode.

The CV values for the two flight modes were 26.5% and 30.0%, respectively, both falling within the acceptable range of dispersion for engineering experiments. In the normal mode, the flight path is automatically executed by the flight control system, which theoretically ensures higher operational consistency; the main sources of data variability in this mode are external environmental factors, such as wind speed fluctuations and GPS positioning errors. In contrast, the slung-load mode is manually piloted, and in addition to environmental factors, the data variability is further compounded by inconsistencies in piloting techniques—e.g., differences in acceleration/deceleration rates and control stick precision—resulting in a slightly higher CV and a somewhat broader data spread compared with the normal mode. Despite these differences, no equipment anomalies or violations of experimental conditions were observed in either group; consequently, all data points were retained to serve as the basis for subsequent analyses of flight mode effects.

Although both groups exhibited relatively high CV values (26.5% for the normal mode and 30.0% for the slung-load mode), the absolute magnitudes of the swing angles in both groups remained small (means of approximately 11–12°), with no peak swing angle exceeding 18°. This indicates that under the 15 kg payload condition, both flight modes are capable of effectively controlling load swing. The elevated swing angle observed in the second flight of the slung-load mode is attributable to the inherent uncertainty of manual control; however, this value still falls within the range of normal physical fluctuations and should therefore be retained in the dataset.

(3) Data Stability under Different Velocity Profiles

Experiment 3 compared the effects of two velocity profiles, namely the S-shaped velocity profile and the trapezoidal velocity profile, on the load swing angle. Both conditions were configured with a 15 kg payload, the normal flight mode, and a swing suppression angle of 10°. The peak swing angle data and descriptive statistics for the two velocity profiles are presented in Table 4.

Table 4. Descriptive statistics of peak swing angle for each group in Experiment 3.

Velocity Profile	n	Peak Swing Angle (°)	Mean (°)	Standard Deviation (°)	Min (°)	Max (°)	Range (°)	CV (%)
S-shaped velocity profile	5	26.25, 24.97, 23.92, 23.56, 14.34	22.61	4.84	14.34	26.25	11.91	21.4
Trapezoidal velocity profile	5	19.50, 24.15, 19.83, 25.78, 19.77	21.81	2.93	19.50	25.78	6.28	13.4

For the S-shaped velocity profile, the mean peak swing angle across five flights was 22.61°, with a standard deviation of 4.84° and a coefficient of variation (CV) of 21.4%. An examination of the raw data shows that the first four flights were highly consistent, ranging from 23.56° to 26.25° with a range of only 2.69°, whereas the fifth flight (14.34°) was notably lower, approximately 10.34° below the mean of the first four flights (24.68°), which is the primary cause of the relatively large standard deviation in this group. Although this particular flight yielded a lower result, no equipment anomalies or sudden meteorological changes were recorded during the experiment. A plausible explanation is that the S-shaped velocity profile, which features a gradual acceleration change during the deceleration phase, may lead to a reduced peak swing response in individual runs due to minor variations in wind conditions or initial attitude. Given that this data point was obtained under experimental conditions identical to those of the other four flights and falls within the normal range of physical fluctuation, it is not treated as an outlier and is retained for subsequent statistical analysis.

For the trapezoidal velocity profile, the mean peak swing angle across five flights was 21.81°, with a standard deviation of 2.93° and a CV of 13.4%. The raw data show that the five results ranged from 19.50° to 25.78°, with a range of 6.28° and no apparent outliers, indicating a relatively balanced data distribution. This group exhibits one of the lowest CV values among all experimental groups (tied with the 10° swing suppression angle group), suggesting that despite its higher rate of velocity change, the trapezoidal velocity profile produces consistent peak swing responses under the 15 kg payload condition, with good repeatability.

The CV of the trapezoidal velocity profile group (13.4%) is markedly lower than that of the S-shaped velocity profile group (21.4%), indicating that the trapezoidal profile yields more repeatable excitation responses under the given payload condition. Although the S-shaped profile group exhibits greater intra-group dispersion due to one comparatively low result, this data point remains within the normal range of physical variability and should be retained. Overall, both datasets are considered suitable for subsequent inter-group comparative analyses.

(4) Data Stability under Different Swing Suppression Angles

Experiment 4 compared the effects of three swing suppression angles, 10°, 30°, and 50°, on the load swing angle. All three conditions were configured with a 15 kg payload, the normal flight mode, and a trapezoidal velocity profile. The data for the 10° condition were adopted from the trapezoidal velocity profile group in Experiment 3, as the experimental conditions (15 kg payload, normal flight mode) were identical except for the velocity profile, and the swing suppression angle was explicitly set to 10° in Experiment 3; therefore, the data are consolidated for use. The peak swing angle data and descriptive statistics for the three swing suppression angle conditions are presented in Table 5.

Table 5. Descriptive statistics of peak swing angle for each group in Experiment 4.

Swing Suppression Angle	n	Peak Swing Angle (°)	Mean (°)	Standard Deviation (°)	Min (°)	Max (°)	Range (°)	CV (%)
10°	5	19.50, 24.15, 19.83, 25.78, 19.77	21.81,	2.93	19.50	25.78	6.28	13.4
30°	3	16.40, 19.61, 12.57	16.19	3.55	12.57	19.61	7.04	21.9
50°	4	15.04, 16.95, 19.19, 18.91	17.52	1.93	15.04	19.19	4.15	11.0

Among the three groups, the 50° condition exhibits the best repeatability (CV = 11.0%), followed by the 10° condition (CV = 13.4%). The 30° condition shows a slightly higher CV of 21.8%, which is attributable to its smaller sample size (n = 3) and the presence of one relatively low value (12.57°); nevertheless, this value remains within the acceptable range for engineering experiments. In terms of mean values, the 10° group yields a significantly higher mean (21.81°) than the 30° group (16.19°) and the 50° group (17.52°), whereas the means of the 30° and 50° groups are relatively close to each other. Regarding the coefficient of variation, the intra-group dispersion across the three swing suppression angle conditions exhibits a trend of first increasing and then decreasing with increasing swing suppression angle. This may be attributed to the enhanced nonlinearity of the attitude compensation of the flight control system as the swing suppression angle increases.

In summary, the coefficients of variation for all nine experimental groups fall within the acceptable range (CV < 30%), and no outliers requiring exclusion due to equipment malfunction or operational errors are identified. For groups with CV values exceeding 20% (e.g., the 6 kg payload, the two flight modes, the S-shaped velocity profile, and the 30°/50° swing suppression angle conditions), the observed dispersion primarily stems from physical factors—such as differences in load inertia, randomness in manual control, environmental disturbances, and nonlinear dynamic responses—rather than measurement errors. Therefore, all experimental data are considered sufficiently reliable for subsequent inter-group statistical analyses.

4.1.2. Inter-Group Statistical Analysis

Based on the data stability analysis in the preceding subsection, which confirms that each dataset possesses sufficient reliability, statistical tests are performed in this section to examine inter-group differences under the influence of each experimental factor. In accordance with the characteristics of each dataset, non-parametric test methods are uniformly adopted to circumvent the issue of violated normality assumptions under small sample sizes. The significance level is set at $\alpha = 0.05$ for all tests, and both the test statistic and the corresponding p-value are reported for each comparison to determine the statistical significance of the differences. Inter-group difference analyses are conducted on all experimental data, and the resulting technical indicators are summarized in Table 6.

Table 6. Summary of inter-group difference test results.

Experiment No.	Comparison Groups	Sample Sizes	Test Method	Test Statistic	p-Value	Significance
Experiment 1	6 kg vs. 15 kg	5, 3	Mann–Whitney U	U = 4	>0.05	Not significant
Experiment 2	Normal mode vs. Slung-load mode	5, 5	Mann–Whitney U	U = 11	>0.05	Not significant
Experiment 3	S-shaped vs. Trapezoidal velocity profile	5, 5	Mann–Whitney U	U = 10	>0.05	Not significant
Experiment 4	10° vs. 30° vs. 50°	5, 3, 4	Kruskal–Wallis	H = 7.08	0.029	Significant
Experiment 4 (post hoc)	10° vs. 50°	—	—	Z = 2.53	0.033	Significant
Experiment 4 (post hoc)	10° vs. 30°	—	—	Z = 1.71	0.261	Not significant
Experiment 4 (post hoc)	30° vs. 50°	—	—	Z = 0.74	1.000	Not significant

(1) Effect of Payload Mass on Peak Swing Angle

Although the mean value of the 6 kg group (26.81°) was numerically higher than that of the 15 kg group (22.55°), the Mann–Whitney U test indicated that the difference between the two groups did not reach statistical significance (U = 4, $p > 0.05$). This result is primarily attributable to two factors: first, the 6 kg group exhibited considerable intra-group dispersion (CV = 27.9%), with one notably low value (14.51°) and one notably high value (35.71°), which led to a dispersed rank distribution and lowered the overall rank sum of the group; second, the 15 kg group had a sample size of only three, yielding limited statistical power to capture any potential true difference.

Although not statistically significant, from an engineering perspective, the mean value of the 15 kg group (22.55°) was approximately 15.9% lower than that of the 6 kg group (26.81°), and the coefficient of variation in the 15 kg group (12.9%) was markedly superior to that of the 6 kg group (27.9%), indicating that increasing the payload mass contributes to reducing the peak swing angle and improving flight consistency. This trend is consistent with theoretical analysis: a heavier payload possesses greater inertia, resulting in smaller angular acceleration responses under identical acceleration excitations, and exhibits enhanced resistance to external disturbances. It is recommended that future studies increase the number of replicates for the 15 kg group (to five) to further verify the statistical significance of this trend.

(2) Effect of Flight Mode on Peak Swing Angle

The Mann–Whitney U test revealed that the difference in peak swing angle between the normal mode (mean = 11.32°) and the slung-load mode (mean = 12.21°) was not statistically significant (U = 11, $p > 0.05$). The means of the two flight modes differed by only 0.89°, which constitutes a negligible difference from an engineering standpoint.

Although no statistically significant difference was observed, the advantages and disadvantages of the two flight modes are manifested in practice. In the normal mode, the flight path is automatically executed by the flight control system, providing good flight consistency; however, the fixed deceleration parameters during the deceleration phase may induce abrupt load swings (the difference between the second flight at 8.71° and the third flight at 14.14° in the normal mode group was 5.43°, reflecting a certain degree of randomness in the excitation during automatic deceleration). In contrast, the slung-load mode is manually controlled, allowing the pilot to adjust the control strategy in real time based on visual observation of the load swing state, and a more gradual deceleration can be applied to avoid large-amplitude swings (apart from the second flight at 17.49°, the remaining four flights in the slung-load mode group were all within 13.33°). Nevertheless, the slung-load mode demands a higher level of pilot skill; the maximum value of 17.49° observed in this group resulted from less refined control inputs during the second flight.

(3) Effect of Velocity Profile on Peak Swing Angle

The Mann–Whitney U test indicated that the difference in peak swing angle between the S-shaped velocity profile (mean = 22.61°) and the trapezoidal velocity profile (mean = 21.81°) was not statistically significant (U = 10, $p > 0.05$), and this conclusion remained unchanged after excluding the outlier of 14.34°. The mean value of the S-shaped profile group was only 0.80° higher than that of the trapezoidal profile group, a minor difference that cannot be statistically attributed to the velocity profile.

The S-shaped velocity profile is designed to smooth acceleration changes and theoretically reduce peak acceleration excitation, thereby decreasing load swing. However, the experimental results reveal no significant difference between the two profiles in terms of peak swing angle. Combined with the data stability analysis, the S-shaped profile group exhibited a larger standard deviation (4.84°) than the trapezoidal profile group (2.93°), suggesting that the former is more susceptible to external conditions. This finding implies that, in actual flight, even when a smoother S-shaped velocity profile is adopted, smoothing the velocity profile alone may not be sufficient to significantly reduce the peak swing angle without active swing suppression control. In contrast, although the trapezoidal velocity profile features a higher rate of velocity change, its excitation pattern is straightforward and yielded more consistent responses. This provides a reference for velocity planning in flight control systems: Given the existing swing suppression mechanism, the optimization margin for velocity profiles may be limited, and a more effective strategy would be to optimize the swing suppression angle or introduce closed-loop feedback control.

(4) Effect of Swing Suppression Angle on Peak Swing Angle

The Kruskal–Wallis test indicated a significant overall difference in peak swing angle among the three swing suppression angle groups (H = 7.19, $p = 0.027$). However, after Bonferroni correction, none of the pairwise comparisons in the Dunn post hoc test reached statistical significance (corrected $p > 0.05$). This result suggests that, although the overall distributions of the three groups differ, the statistical power of the post hoc tests is limited by the small sample sizes (particularly the 30° group, with only three replicates) and the considerable overlap in rank orders among the groups. In terms of numerical trends, the mean value of the 10° group (21.81°) was substantially higher than those of the 30° group (16.19°) and the 50° group (17.52°), whereas the difference between the 30° and 50° groups was minimal (only 1.33°), indicating that increasing the swing suppression angle to 30° yields the primary suppression effect, and further increasing it to 50° does not provide additional significant improvement.

The swing suppression angle is a core control parameter in the flight control system for mitigating load swing, essentially defining the maximum allowable attitude adjustment angle when the system detects load oscillation. The experimental results show that increasing the swing suppression angle from 10° to 30° reduced the mean peak swing angle by approximately 5.62° (a 25.8% reduction), whereas further increasing it to 50° resulted in a slight increase in the mean value relative to the 30° group (by 1.33°), though still substantially lower than that of the 10° group. This non-monotonic trend suggests that 30° may be the optimal swing suppression angle setting for the UAV system under the conditions of a 15 kg payload, the slung-load mode, and a trapezoidal velocity profile. An excessively large suppression angle (50°) may introduce additional coupling effects due to overcompensation in attitude adjustment, which could be counterproductive for swing suppression. In terms of data stability, the 50° group exhibited the best repeatability (CV = 11.0%), indicating consistent system responses under this parameter, although its mean value did not outperform that of the 30° group.

Based on the flight data from four sets of experiments, this section presents a systematic stability analysis and inter-group difference testing of the peak swing angle of the UAV slung-load system under varying payload masses, flight modes, velocity profiles, and swing suppression angles. The main conclusions are as follows:

The coefficients of variation (CV) for all nine experimental groups were below 30%, with the 50° swing suppression angle group (CV = 11.0%) and the 15 kg payload group (CV = 12.9%) exhibiting the best repeatability, indicating that a heavier payload and a properly configured swing suppression angle contribute to improved flight consistency. Certain groups (e.g., 6 kg payload, normal/slung-load modes, S-shaped velocity profile, and 30° swing suppression angle) showed CV values ranging from 20% to 27%, reflecting moderately higher dispersion; however, the physical causes are well understood, and no outliers warranting exclusion were identified. All data are therefore considered suitable for subsequent statistical comparisons.

Among the four experimental factors investigated, only the swing suppression angle exerted a statistically significant effect on the peak swing angle (Kruskal–Wallis test, H = 7.19, $p = 0.027$). However, none of the pairwise comparisons in the Dunn post hoc test with Bonferroni correction reached significance, suggesting that the overall difference among the three groups primarily arises from the separation of the 10° group from the 30°/50° groups, while the pairwise differences are not sufficiently robust, possibly limited by the small sample sizes (particularly the 30° group, n = 3). The effects of payload mass, flight mode, and velocity profile on the peak swing angle did not reach statistical significance.

Although most inter-group comparisons did not reach statistical significance, the numerical trends provide clear engineering guidance: increasing the payload mass from 6 kg to 15 kg reduced the mean value by approximately 15.9%; the mean difference between the two flight modes was less than 1°; the mean difference between the two velocity profiles was less than 1°; and increasing the swing suppression angle from 10° to 30° reduced the mean value by approximately 25.8%, whereas further increasing it to 50° resulted in a mean value of 17.52°, with only a minor difference from the 30° group (16.19°). This indicates that 30° may be the optimal swing suppression angle for the UAV-payload system, effectively suppressing swing while avoiding the adverse effects of excessive attitude compensation.

These findings suggest that, within the existing framework of industrial-grade UAV flight control systems, proper configuration of the swing suppression angle is the most effective and readily implementable approach for improving load swing stability. It is recommended that in engineering practice, 30° be adopted as the baseline value, with fine-tuning within the range of 20° to 40° based on mission requirements (e.g., flight speed and payload type). Meanwhile, although payload mass, flight mode, and velocity profile did not exhibit statistically significant effects, their synergistic effects on system response warrant further investigation in future studies.

4.2. Effect of Payload Mass on Swing Angle

A 330 m straight-line path was planned for the UAV via the ground station, with the normal flight mode, a trapezoidal velocity profile, and the swing suppression angle set at 30°. The experimental loads were divided into two groups: 6 kg and 15 kg respectively. According to the data collected by the IMU module, the maximum average swing angle Φ_{max}, stabilization time T, and confidence intervals are shown in Table 7:

Table 7. Key Indicators of UAV Attitude Changes in Experiment 1.

Suspended Load (kg)	Maximum Average Swing Angle ± Standard Deviation (°)	Maximum Stabilization Time T (s)	Confidence Interval (Confidence Level 95%)
6	24.03 ± 14.51	14	(13.93, 34.13)
15	18.49 ± 2.42	16	(11.39, 25.59)

The average swing angle was calculated from five experimental runs. The average swing angle, standard deviation, margin of error, and error bars during the flight are shown in Figure 6.

As can be seen from the speed and swing angle response curve in Figure 6, when the load is 6 kg, a relatively large swing angle occurs for the suspended load every time the UAV accelerates or decelerates. When the UAV accelerates from 0 m/s to 3 m/s, the swing angle appears instantaneously. The maximum swing angle at takeoff is 11.05°. Subsequently, the UAV travels at a constant speed of 3 m/s, and the swing of the suspended load gradually stabilizes after 15 s. When the UAV accelerates for the second time, from 3 m/s to 5 m/s, the maximum swing angle is 12.13°. After reaching a constant-speed state of 5 m/s, the swing of the suspended load gradually stabilizes. During the third speed change, when the UAV decelerates from 5 m/s to 3 m/s, the maximum swing angle is 24.03°, and the suspended load gradually stabilizes after 14 s. Finally, when the UAV reaches the destination and its speed drops to 0 m/s, the swing angle increases to 10.48° during deceleration. From the changing trends of the average value, standard deviation, and margin of error in above figure, it can be seen that the three have similar changing trends. As the swing angle increases, the standard deviation and margin of error also increase, intensifying the uncertainty of the system.

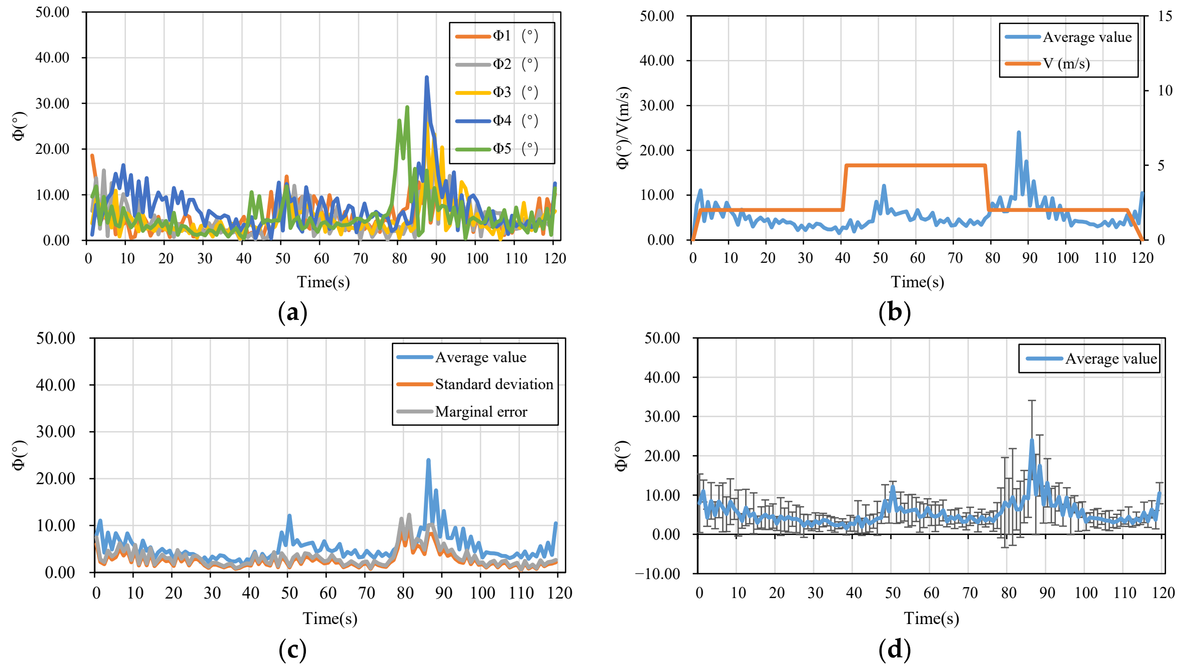

Figure 6. Swing angle response curve of the UAV with a 6 kg suspended load. (**a**) Variation curves of the swing angle for each flight trial. (**b**) Average swing angle-speed change curve. (**c**) Curves of the average value, standard deviation and marginal error of the swing angle. (**d**) Error bars of average swing angle.

Figure 7 shows the speed and swing angle response curve when the load is 15 kg. The variation trend of the swing angle is similar to that of the 6 kg load. When the UAV accelerates from 0 m/s to 3 m/s, the swing angle occurs instantaneously, with the maximum swing angle at takeoff being 10.50°. When the UAV accelerates for the second time, from 3 m/s to 5 m/s, the maximum swing angle is 11.20°, and then the suspended load continues to oscillate. During the third speed change, when the UAV decelerates from 5 m/s to 3 m/s, the maximum swing angle is 18.49°, and the suspended load gradually stabilizes after 16 s. Finally, when the UAV reaches the destination and its speed drops to 0 m/s, the swing angle at the end point is 5.54°. From the changing trends of the average value, standard deviation, and margin of error in the above figure, it can be seen that the three have similar changing trends. As the swing angle increases, the standard deviation and margin of error also increase, intensifying the uncertainty of the system.

According to the results of the two groups of experiments, it can be seen that the suspended load with a larger mass (15 kg) generates a relatively smaller swing angle. From Equations (25) and (26), it can be seen that $\ddot{\theta}_x$ and $\ddot{\theta}_y$ are coupled with the mass m of the suspended load. Taking Equation (25) as an example, we rearrange it into the form about $\ddot{\theta}_x$

$$\ddot{\theta}_x = \frac{mlS_xS_y\ddot{x} + mlC_x\ddot{y} + mlC_yS_x\ddot{z} - ml^2S_xC_x\dot{\theta}_y^{\,2} - mlgS_yC_y}{I_p + ml^2} \tag{28}$$

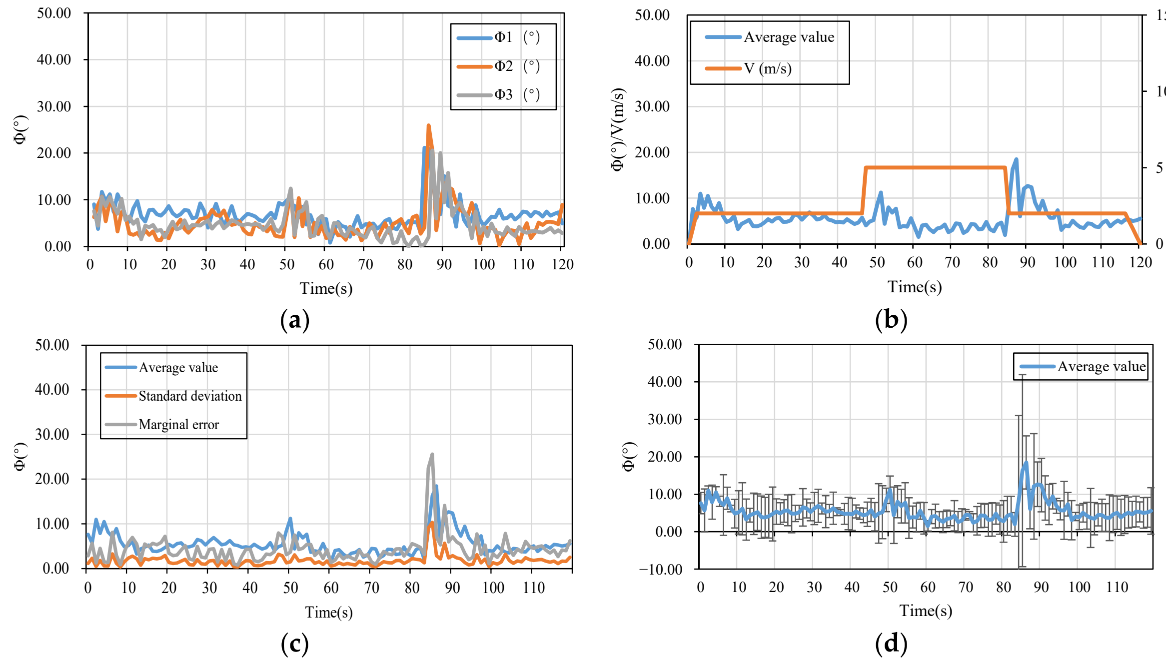

Figure 7. Swing angle response curve of the UAV with a 15 kg suspended load. (**a**) Variation curves of the swing angle for each flight trial. (**b**) Average swing angle-speed change curve. (**c**) Curves of the average value, standard deviation and marginal error of the swing angle. (**d**) Error bars of average swing angle.

As can be seen from the above formula, when m increases, both the numerator and the denominator increase in the same order as m, but the ml^2 term in the denominator will suppress the amplifying effect of $\ddot{\theta}_x$. Therefore, under the same acceleration-deceleration excitation of the UAV, as the mass of the load increases, the angular acceleration of the swing angle $\ddot{\theta}_x$ and $\ddot{\theta}_y$ decreases, the growth rate of the swing angle becomes slower, and the peak swing angle is lower.

In addition, the 15 kg suspended load with a larger mass has a longer convergence and stabilization time, and the swing angle during the stable period is relatively larger than that of the 6 kg suspended load. According to the simple pendulum theory, we know that the convergence speed of the swing depends on the ratio of the equivalent damping to the moment of inertia. From the denominator $I_p + ml^2{C_y}^2$ of the above Formula (28), it can be seen that the larger m is, the larger the equivalent moment of inertia is, the stronger the inertia of the swing is, and the slower the swing decays.

Furthermore, as can be seen from Figures 6 and 7, the average value, standard deviation, and margin of error exhibit the same trend of change. As the swing angle increases, the standard deviation and margin of error also increase, intensifying the uncertainty of the system. From the Lagrangian dynamic Equation (25) of the load swing, when the swing angle is small, $C_x \approx 1, S_x \approx \theta_x, C_y \approx 1, S_y \approx \theta_y$. The trigonometric functions can be approximated in a linear form. When the system coupling terms are weak, the equivalent moment of inertia is approximately constant, the trajectory predictability is strong, and the standard deviation and margin of error of the swing are small. As the swing angle increases, the non-linear deviation of the trigonometric functions, the coupling effect, and the time-varying characteristics of the equivalent moment of inertia are all amplified. The influence of parameter errors and external disturbances is exponentially amplified by the non-linear mechanism. At the same time, the error transfer effect of multi-dimensional swings is enhanced. Eventually, the standard deviation and margin of error of the swing angle increase significantly, and the overall uncertainty of the system intensifies.

In this experiment, the maximum swing angle of the 15 kg payload is reduced by 23.05% compared with that of the 6 kg payload, whereas the settling time is prolonged by 14.28%. This phenomenon is attributed to the combined effects of classical physical laws and the specific dynamic coupling inherent in the UAV-payload suspension system. Firstly, the increase in the load moment of inertia directly enhances the system's ability to resist angular acceleration disturbances. According to Newton's second law, under the same drone movement excitation, a heavier load generates a smaller swing angular displacement, which is consistent with the laws of pendulum motion. However, a more important mechanism lies in the relative change in system damping. The swing attenuation mainly depends on air damping and the inherent passive damping of the system. When the load mass rises, the system's stored kinetic energy increases. But the damping-dissipated power does not increase proportionally. This causes the system's equivalent damping ratio to drop, lengthening the swing attenuation process. This is essentially a trade-off between "amplitude-speed", reflecting the dynamic balance between energy input and dissipation rates. In the existing theoretical research, when deriving the dynamic equations, the influence of the mass parameter on the system inertia and natural frequency is generally acknowledged. However, in most literature on Lyapunov-stability or differential-flatness-based controller design [20,28], stability proof often assumes the load mass is known or constant. It does not deeply explore how mass changes quantitatively affect the transient response. Some adaptive-control studies aim to estimate mass online for control performance [40]. But they focus on controller robustness, not giving quantitative operational-strategy guidance [41]. This paper's empirical conclusions fill this gap. They turn the abstract mass parameter in the theoretical model into a quantitative relationship, which directly guides practical operations.

Based on the analysis of Experiment 1, the following strategies are recommended. For scenarios with tiny spatial swing tolerances (like aerial surveys, precision installations, high-end equipment transport), within the drone's safety and power limits, use counterweights or combined transport. This makes the actual load near the max allowable, leveraging inertia suppression. For high-timeliness delivery scenarios (like emergency rescue, rapid medical transfers, urban instant delivery), use lightweight packaging and design. You can even do multiple small-batch transports to get the shortest in-air stabilization and hovering times. But note the suggestions' boundaries. Our conclusions rely on a linear rope-length model. When the load nears the drone's max thrust limit, the disc load for altitude changes the dynamic response. This might cause opposite-direction swing surges. So, the "increase weight to stabilize amplitude" strategy's effective boundary is well below the max load; more experiments are needed. Also, emphasize the scene-coupling boundary. In strong winds or complex airflows, a larger load's inertia advantage may be offset by aerodynamic interference. Then, re-evaluate the "amplitude-priority strategy" benefits.

This section discusses the influence of different suspended-load masses on the swing of the suspended load. As can be seen from Figure 8, when the UAV is operated in the normal flight mode with a trapezoidal velocity profile and the swing suppression angle set to 30°, an increase in the slung load from 6 kg to 15 kg results in a decrease in the maximum swing angle by approximately 23.05%, whereas the settling time of the swing angle exhibits a certain increase of about 14.28%. In addition, the deviation and dispersion degree of the swing angle increase with the increase in the swing angle. Based on the above experimental conclusions, suspended-load UAVs should choose different flight strategies according to different application scenarios. When the requirement for the swing amplitude of the UAV is high, such as for aerial survey UAVs and photography UAVs, the mass of the suspended load should be appropriately increased to control the maximum swing angle of the UAV. When the requirement for the swing time of the UAV is short, such as in emergency rescue and urban logistics distribution, the weight of the load should be appropriately reduced to achieve rapid delivery.

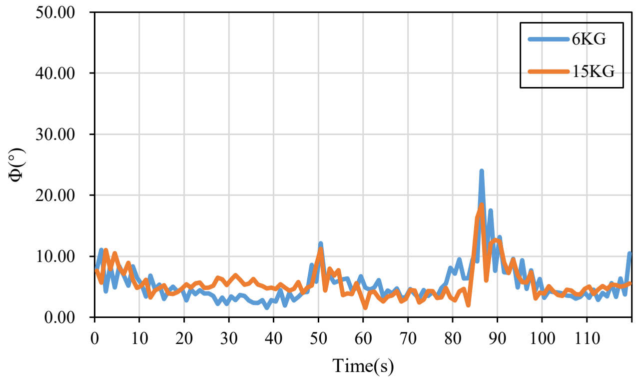

Figure 8. Weight-swing angle response curve of the UAV with a suspended load.

4.3. Effect of Flight Mode

A 130 m straight-line flight path was planned for the UAV via the ground station. The UAV carried a 15 kg slung load, with the swing suppression angle set to 30° and a trapezoidal velocity profile adopted. Two sets of flight experiments were conducted, using the slung-load mode and the normal mode, respectively. The attitudes of the suspended load in the two flight modes were recorded respectively. The maximum swing angles and settling times obtained from the post-processing of the data collected by the IMU module are shown in Table 8.

Table 8. Key Indicators of UAV Attitude Changes in Experiment 2.

Flight Modes	Maximum Average Swing Angle ± Standard Deviation (°)	Maximum Stabilization Time *T* (s)	Confidence Interval (Confidence Level 95%)
Suspended load mode	8.36 ± 3.58	7	(4.78, 11.94)
Normal mode	7.19 ± 5.11	6	(2.07, 12.30)

The flight of the UAV in the suspended-load mode requires the pilot to manually control throughout the process. As can be seen from the speed and swing-angle response curve in Figure 9, when the UAV takes off in the suspended-load mode and accelerates from 0 m/s to 1 m/s, the suspended load keeps swinging. During the second acceleration from 1 m/s to 3 m/s, the pilot accelerates at the maximum power, and the swing angle generated at this time is the largest, with the maximum value of 8.36°. The swing of the suspended load gradually stabilizes after 7 s. During the third speed change, when the UAV decelerates from 3 m/s to 0 m/s, the pilot decelerates slowly. The swing angle of the suspended load does not change drastically, with the maximum swing angle of 4.46°. As the speed of the UAV decreases, the swing angle of the suspended load also converges.

In the normal mode, the UAV flies automatically along the route designed by the ground station. As can be seen from Figure 10, the maximum swing angle of the UAV during takeoff is 7.19°. The suspended load keeps oscillating from takeoff until the speed reaches 3 m/s. After reaching the maximum swing angle, the UAV enters a uniform-speed flight, and the swing angle of the suspended load starts to converge after approximately 6 s. Finally, when the UAV approaches the end point, it decelerates rapidly. At this moment, the suspended load swings violently, generating a maximum swing angle of about 9.70°.

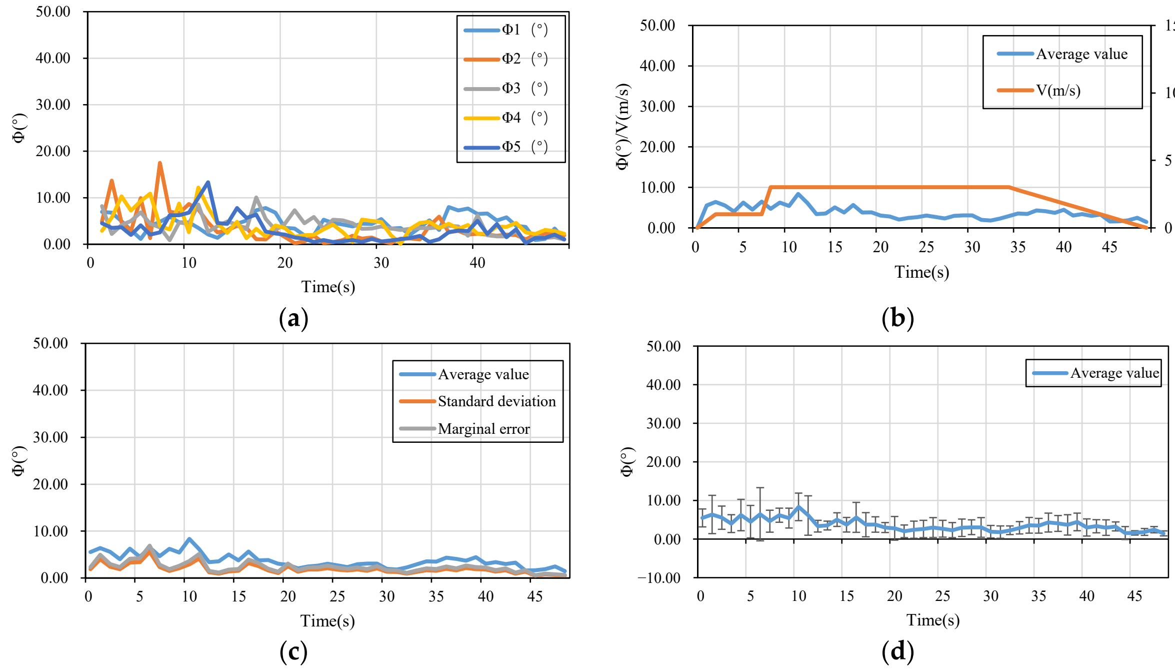

Figure 9. Swing angle state responses under Suspended load mode. (**a**) Variation curves of the swing angle for each flight trial. (**b**) Average swing angle-speed change curve. (**c**) Curves of the average value, standard deviation and marginal error of the swing angle. (**d**) Error bars of average swing angle.

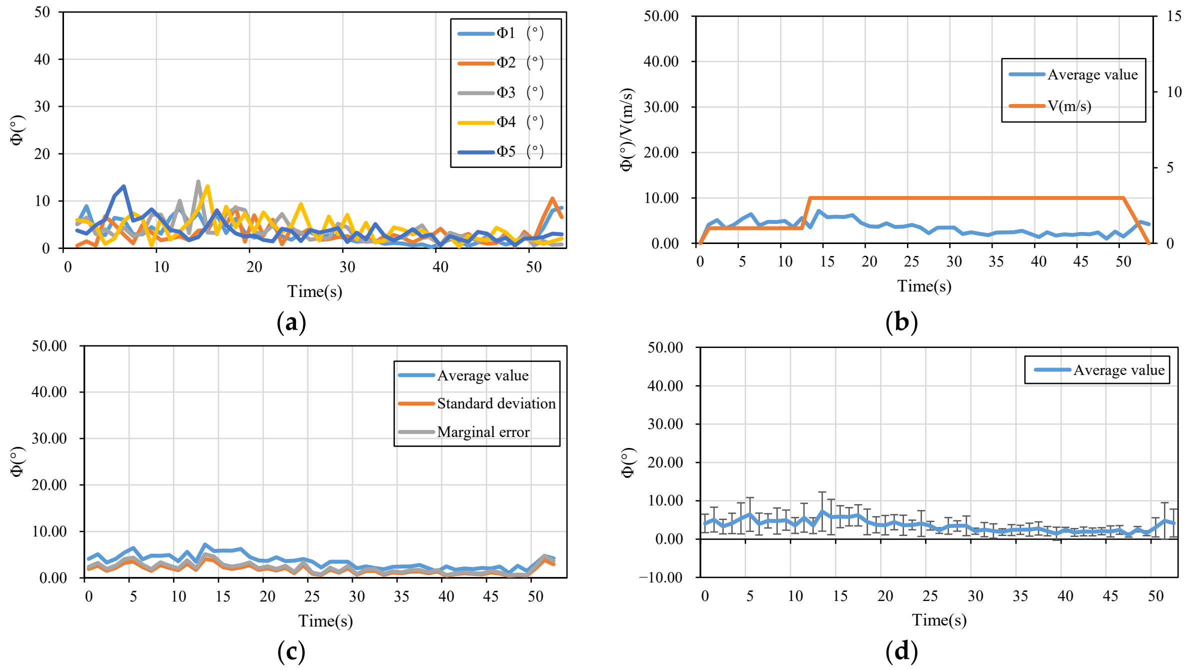

Figure 10. Swing angle state responses under Normal mode. (**a**) Variation curves of the swing angle for each flight trial. (**b**) Average swing angle-speed change curve. (**c**) Curves of the average value, standard deviation and marginal error of the swing angle. (**d**) Error bars of average swing angle.

Figure 11 shows the speed-swing-angle curves comparison between the suspended-load mode and the normal mode, it can be seen that in the suspended-load mode, the UAV can achieve slow deceleration during the deceleration phase, and the suspended load does not swing violently. The maximum swing angle of the suspended load decreases from 8.36° to 7.19°, with the amplitude of the swing angle reduced by 14%.

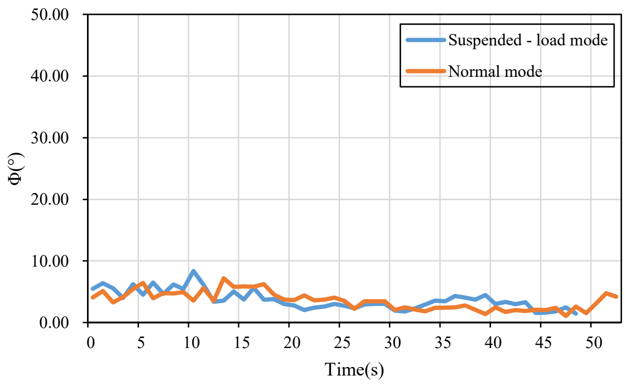

Figure 11. Swing angle state responses under different flight modes.

According to Experiment 2, the essence of the flight mode is the difference in the effectiveness of open-loop planning and closed-loop feedback. In the suspended-load mode, the UAV generates a relatively large swing angle during the acceleration phase and a relatively small swing angle during the deceleration phase. In the normal mode, relatively large swing angles are generated during both the acceleration and deceleration phases. The root cause lies in the fundamental differences in their underlying control architectures. The manual operation of the suspension mode essentially introduces a highly adaptive and predictive human–eye–human–brain feedback closed loop. An experienced pilot can monitor the load swing in real-time. Using forward-looking and flexible throttle and attitude control, they can perform operations like input shaping or energy dissipation to actively counter the swing energy. The "normal mode" relies on the position-velocity-PID control loop built into the flight control system. Its primary design goal is the trajectory tracking of the UAV itself, and the suppression of load swing is a passive response based on a pre-set model. The large swing angle during deceleration and the gradual change during constant speed clearly show the steady-state error or limit cycle in the controller. This occurs when the controller handles the system's strong coupling and non-linearity. This is an inherent limitation of classical linear PID control in dealing with such under-actuated systems. At present, the research goals of many advanced control studies, such as passivity-based control, geometric control, and back-stepping control, are to design an automated controller that is globally stable and free of static error, like an excellent pilot [28,31,42]. The experimental results of this paper provide the most direct evidence for the necessity of these advanced algorithms: The steady-state error of the normal mode indicates that the commercial-grade general-purpose flight control has insufficient performance when facing the suspension system. At the same time, the experiment also quantifies the upper limit of performance that humans as controllers can achieve, which provides a valuable gold reference standard for evaluating the performance of autonomous driving algorithms.

Based on the analysis of Experiment 2 above, the following strategies and suggestions can be obtained. Optimize the allocation of human resources and establish a pilot dispatch system based on the value and stability requirements of the goods. The transportation tasks of high-value and vulnerable goods, such as precision instruments and artworks, must be carried out by high-level pilots, and the suspension mode must be used; optimize the operation process. When the normal mode is widely applied to logistics distribution, the trajectory of the terminal landing stage must be optimized. Learn from the manual-operation advantages in the experiment. At the end of the automatic flight route, design a swing-elimination section. It can have an extremely slow approach or include a short hover. This gives the system enough time to use its own damping to reduce the residual swing before landing. However, it should be clear that the applicable boundaries of the above suggestions are as follows. The performance of the suspension mode highly depends on the skills and state of the pilot. During long-term flights, in severe weather, or under complex electromagnetic interference, a pilot's reaction and judgment abilities may decline. As a result, their performance could drop significantly, perhaps even falling below that of the normal mode. The remaining steady-state swing angle in the normal mode indicates that for scenarios demanding millimeter-level precise delivery, simply relying on existing commercial flight controls centered around height-fixing and positioning is not viable. Instead, a more advanced control module that directly uses the load state as feedback must be incorporated.

This section discusses the influence of different flight modes on the swing of the suspended load. A comparison between the slung-load mode and the normal mode reveals that, when the UAV carries a 15 kg payload with the anti-swing angle set to 30° and a trapezoidal velocity profile adopted, the UAV generates a larger swing angle during the acceleration phase in the slung-load mode, whereas in the normal mode, significant swing angles occur during both the acceleration and deceleration phases. This is because in the suspended-load mode, through manual control, the UAV can accelerate and decelerate slowly, and this flight method can effectively control the maximum swing angle when the UAV decelerates. In addition, during the take-off phase, due to the pilot using a larger acceleration in the suspended-load mode, the maximum swing angle is significantly larger than that in the normal mode. It can be seen that if the operation is improper during manual flight, a larger swing angle will be generated compared with the normal mode, which requires a higher level of flight skills from the pilot. In view of the above experimental phenomena, the following strategies can be adopted in engineering to reduce the swing amplitude of the suspended load. First, when the stability requirement for the suspended-load delivery is high, it is recommended to use manual-control flight to achieve a gentler acceleration and deceleration through the suspended-load mode. However, the suspended-load mode requires a high level of professional skills from the pilot. Second, when the transportation efficiency requirement is high but the stability requirement is not high, it is recommended to use the normal flight-route mode. At this time, the UAV flies faster and has higher efficiency.

4.4. Effect of Speed Trajectories

The UAV, carrying a 15 kg slung load with the anti-swing angle set to 30°, was flown along a 600 m path in the normal flight mode using two different velocity profiles. The S-curve with slow speed change, adopting a smooth S-shaped speed-curve transition. After the UAV takes off, the speed increases by 2 m/s every 60 m, and after the speed reaches 10 m/s, it decelerates slowly to 0 m/s; The trapezoidal curve with fast-changing speed. The UAV accelerates rapidly from 0 m/s to 10 m/s, then maintains a constant-speed flight, and after the load swing tends to be stable, it decelerates rapidly to zero. The maximum swing angles and settling times obtained from the post-processing of the data collected by the IMU module are shown in the following Table 9.

Table 9. Key indicators of UAV attitude changes in Experiment 3.

Speed Curve	Maximum Average Swing Angle ± Standard Deviation (°)	Maximum Stabilization Time T (s)	Confidence Interval (Confidence Level 95%)
S-curve	15.04 ± 10.72	Not stabilized	(4.32, 25.75)
Trapezoidal curve	18.78 ± 9.37	Not stabilized	(9.40, 28.15)

As can be seen from Figure 12, the S-shaped speed curve generates a relatively large swing angle whenever the speed changes. The maximum swing angle during the acceleration phase is 15.04°. After the UAV continuously accelerates to the peak speed of 10 m/s, it starts to decelerate step by step. The maximum swing angle during the deceleration process is 20.86°. In the starting stage of the S-shaped speed curve, due to low-speed flight, there is a period of swing-angle convergence. Subsequently, throughout the process, the UAV keeps changing speed, and the suspended load is in a high-level oscillation state, and the swing angle cannot converge.

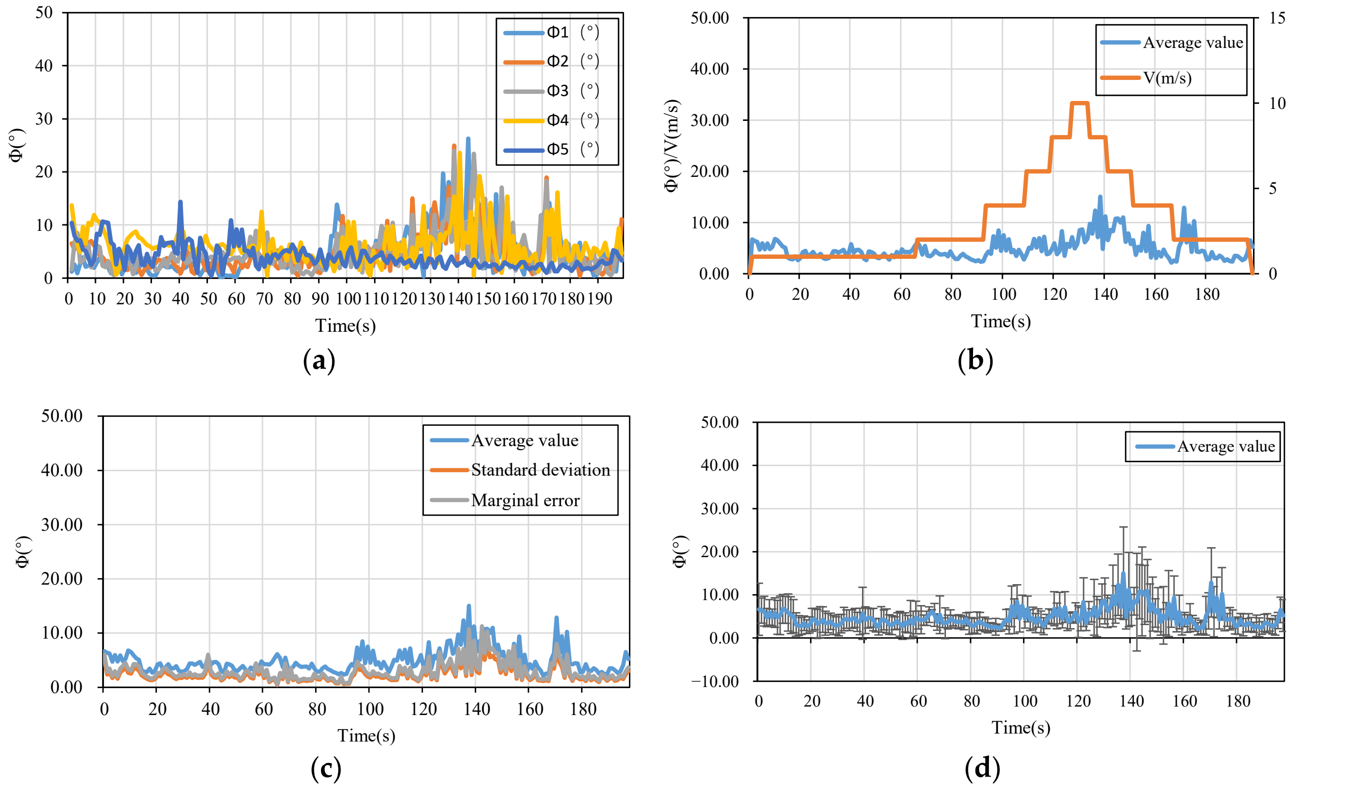

Figure 12. Swing angle state responses under S-speed curves. (**a**) Variation curves of the swing angle for each flight trial. (**b**) Average swing angle-speed change curve. (**c**) Curves of the average value, standard deviation and marginal error of the swing angle. (**d**) Error bars of average swing angle.

As can be seen from Figure 13, the trapezoidal speed curve generates relatively large swing angles when accelerating to 10 m/s and when decelerating from 10 m/s, which are 18.78° and 15.42° respectively. After accelerating to the maximum speed, the suspended load experiences a brief period of stability and then fluctuates again. Due to the relatively high constant-speed flight speed, the swing is vulnerable to coupling effects, and the swing angle remains at a relatively large value.

As can be seen from Figure 14, compared with the trapezoidal speed curve, the S-shaped speed curve has a smaller acceleration due to its slow speed change, resulting in a smaller extreme value of the swing angle during the acceleration phase. By adopting the S-shaped gentle acceleration method, the amplitude of the swing angle is reduced by 19.91%.

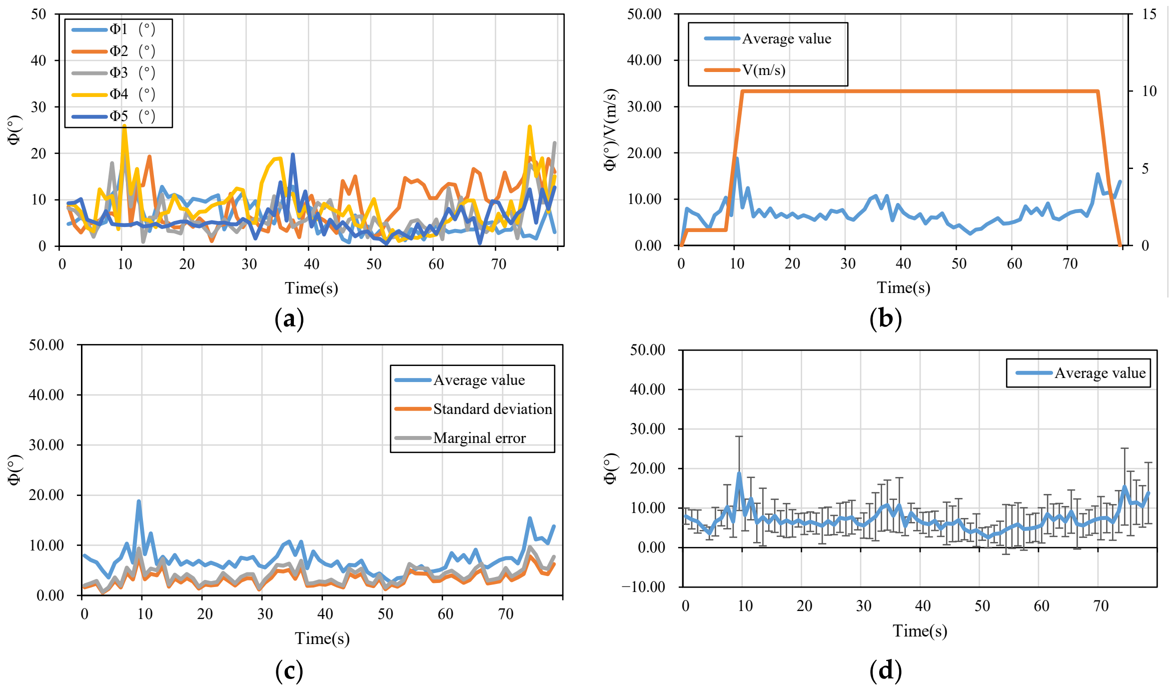

Figure 13. Swing angle state responses under Trapezoidal curves. (**a**) Variation curves of the swing angle for each flight trial. (**b**) Average swing angle-speed change curve. (**c**) Curves of the average value, standard deviation and marginal error of the swing angle. (**d**) Error bars of average swing angle.

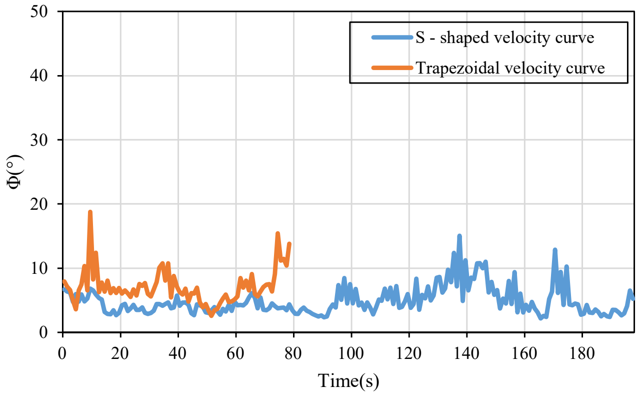

Figure 14. Swing angle state responses under different speed curves.

Analysis: From the transformed form (27) of the Lagrangian dynamic equation, $\ddot{\theta}_x$ and $\ddot{\theta}_y$ are the angular acceleration responses of the load swing. The linear accelerations $\ddot{x}, \ddot{y}, \ddot{z}$ of the UAV are the direct excitation sources of the load swing. They are converted into the excitation torque around the swing axis through the inertial force components, driving the load to swing. When the restoring torque and the equivalent moment of inertia remain unchanged, the greater the acceleration of the UAV, the stronger the excitation torque, the greater the angular acceleration of the load swing, and the more likely it is to be excited to swing with a large amplitude. As the swing angle increases, the non-linear deviation of the trigonometric functions, the coupling effect, and the dynamic change in the equivalent moment of inertia will further amplify the excitation effect of the acceleration on the swing, intensifying the swing and uncertainty of the system.

In this experiment, the critical effect of velocity is investigated. According to Equation (18), it can be seen that there is a two-way coupling between $\ddot{x}$ and θ_x, θ_y in the equation.

The linear acceleration $\ddot{x}$ of the UAV will directly affect the load swing (excitation term), and the angular acceleration $\ddot{\theta}_x, \ddot{\theta}_y$ and angular velocity $\dot{\theta}_x, \dot{\theta}_y$ of the load will also act back on the force F_x of the UAV. During the acceleration phase, the acceleration term $(M+m)\ddot{x}$ of the UAV is strongly coupled with the swing-angle term. In the case of the trapezoidal curve, the UAV accelerates directly from 0 to 10 m/s. The amplitude of $\ddot{x}$ is large and the rate of change is high. The larger $\ddot{x}$ is, the stronger the inertial excitation torque acting on the load, directly driving the load to generate a larger angular acceleration $\ddot{\theta}_x, \ddot{\theta}_y$, resulting in a significant increase in the peak swing angle (18.78°). While the S-shaped curve adopts a smooth transition, with a small amplitude of $\ddot{x}$ and a gentle change, the inertial excitation torque is weak. Therefore, the angular response of the load is also gentler, and the peak swing angle (15.04°) is 19.91% lower than that of the trapezoidal curve. During the constant-speed phase, $\ddot{x} \approx 0$, and the equation is simplified to

$$F_x = mlC_xC_y\ddot{\theta}_y - mlS_xS_y\ddot{\theta}_x - 2mlS_xC_y\dot{\theta}_x\dot{\theta}_y - mlC_xS_y\dot{\theta}_x^{\,2} - mlC_xS_y\dot{\theta}_y^{\,2} \tag{29}$$

At this time, the force F_x acting on the UAV is completely determined by the swing terms of the load. The trapezoidal curve generates a relatively large initial swing angle and swing angular velocity $\dot{\theta}_x, \dot{\theta}_y$ during the acceleration phase. These angular velocity terms ($\dot{\theta}_x^{\,2}, \dot{\theta}_y^{\,2}, \dot{\theta}_x, \dot{\theta}_y$) are converted into Coriolis force and centrifugal force during the constant-speed phase, continuously exciting the load to swing, forming a positive feedback of "swing-force-swing", which makes it difficult for the swing angle to decay and keeps it in a high-level oscillation state. The *S*-shaped curve, due to the continuous change in speed, causes the UAV to generate continuous active excitation, so the swing angle cannot converge.

Based on the analysis of the above experiments, the following strategies and suggestions can be drawn. Strictly control speed indicators. Write "5 m/s" as the default safe cruising speed threshold for heavy-load and long-rope suspension operations of industrial UAVs into the operation specifications. Secondly, when the flight speed exceeds 5 m/s, the S-shaped speed profile should be adopted as much as possible to strictly control acceleration. After each speed step change, a constant-speed "stabilization period" of no less than 6–8 s should be forcedly inserted, and the length of this period needs to be dynamically calibrated according to the measured swing decay time. However, when implementing the strategy, the speed-rope-length coupling boundary should be clarified. The recommended value of 5 m/s is based on a specific rope length (5 m in the experiment). According to the simple pendulum period formula $T = 2\pi\sqrt{L/g}$, changes in rope length will alter the system's natural frequency, thus changing the critical speed value. Therefore, the speed limit must be calibrated in relation to the rope-length configuration. Secondly, the boundary of energy input should not be ignored. Even if the speed is below 5 m/s, if the UAV performs high-frequency and large-amplitude evasive maneuvers (such as emergency obstacle avoidance), the angular acceleration excitation introduced may still instantaneously trigger large-amplitude swings. Therefore, the speed limit needs to be considered in coordination with the agility limit of the flight control.

This section discusses the effect of velocity profile on the slung-load swing angle. Under the conditions of a 15 kg payload, a swing suppression angle of 30°, and the normal flight mode, the analytical results indicate that the trapezoidal velocity profile results in an approximately 14.3% increase in the maximum swing angle compared with the S-shaped velocity profile. It can be seen that when the speed is relatively high, slow acceleration can effectively control the swing angle during the acceleration phase. In addition, when the UAV is flying at a high speed, the coupling of the forces on the suspended load is enhanced, and the robustness is poor. Therefore, it is difficult for the swing angle of the suspended load to converge during high-speed flight of the UAV. Based on the above conclusions, the following flight strategies can be proposed: (1) When the UAV is flying with a suspended load, the flight speed should not be too high, which can ensure the stability of the suspended load and promote the convergence of the swing angle. (2) If the UAV needs to fly at a high speed, it should gradually accelerate to the predetermined speed during the acceleration phase. A certain settling time should be given to the current speed, and then accelerate again when the suspended load gradually stabilizes.

4.5. Effect of Anti-Swing Parameters

In this experiment, the flight path length of the UAV was set to 600 m, with a slung load of 15 kg and a trapezoidal velocity profile. The UAV was operated in the normal flight mode, and the swing suppression angle was sequentially adjusted to 10°, 30°, and 50° across three separate flight tests. The maximum swing angle and settling time were obtained through post-processing of the data collected by the IMU module, and are presented in Table 10.

Table 10. Key indicators of UAV attitude changes in Experiment 4.

Anti-Swing Parameters (°)	Maximum Average Swing Angle ± Standard Deviation (°)	Maximum Stabilization Time T (s)	Confidence Interval (Confidence Level 95%)
10	18.78 ± 9.37	7	(9.40, 28.15)
30	8.08 ± 1.46	8	(6.61, 9.54)
50	11.21 ± 15.55	14	(−4.35, 26.76)

Swing angle response of the UAV with a 10° swing-elimination angle can be seen from Figure 13; a relatively large swing angle is generated whenever the speed changes. The maximum swing angle during the acceleration phase is 18.78°. After the UAV continuously accelerates to the peak speed of 10 m/s, the largest swing angle occurs during the first deceleration, with a peak value of 11.46°. The swing angle fluctuates significantly during the UAV's constant-speed flight phase.

As can be seen from Figure 15, when the swing-elimination angle is 30°, the maximum swing angle at takeoff changes to 8.08°. After reaching the maximum speed, the UAV flies at a constant speed. During this stage, the swing of the suspended load gradually converges, and the suspended load maintains a relatively stable attitude. When approaching the destination, the UAV starts to decelerate. At this time, the largest swing angle throughout the process occurs, with a maximum value of 18.05°.

As can be seen from the speed-swing-angle curve in Figure 16, the maximum swing angle at takeoff becomes 11.21°. After the UAV reaches its maximum speed and enters the constant-speed flight phase, the swing angle of the suspended load gradually converges and stabilizes. After entering the deceleration phase, the maximum swing angle of the suspended load is 7.81°.

As can be seen from Figure 17, the swing angle experiences significant swings during the take-off acceleration phase and the deceleration phase. The swing of the suspended load under the three anti-swing angles in the experiment shows the following patterns: (1) As the swing-elimination angle increases, the swing angle during the take-off phase first decreases and then increases, while the swing-elimination angle during the deceleration phase continuously decreases. (2) When the swing-elimination angle is 10°, the swing angle fluctuates greatly during the constant-speed flight phase. However, when the anti-swing angles are 30° and 50°, the swing angle fluctuates less during the constant-speed phase. In addition, when the swing-elimination angle is adjusted from 10° to 30°, the swing-angle amplitude decreases by 56.98%, and when it is adjusted from 30° to 50°, the swing-angle amplitude increases by 38.74%.

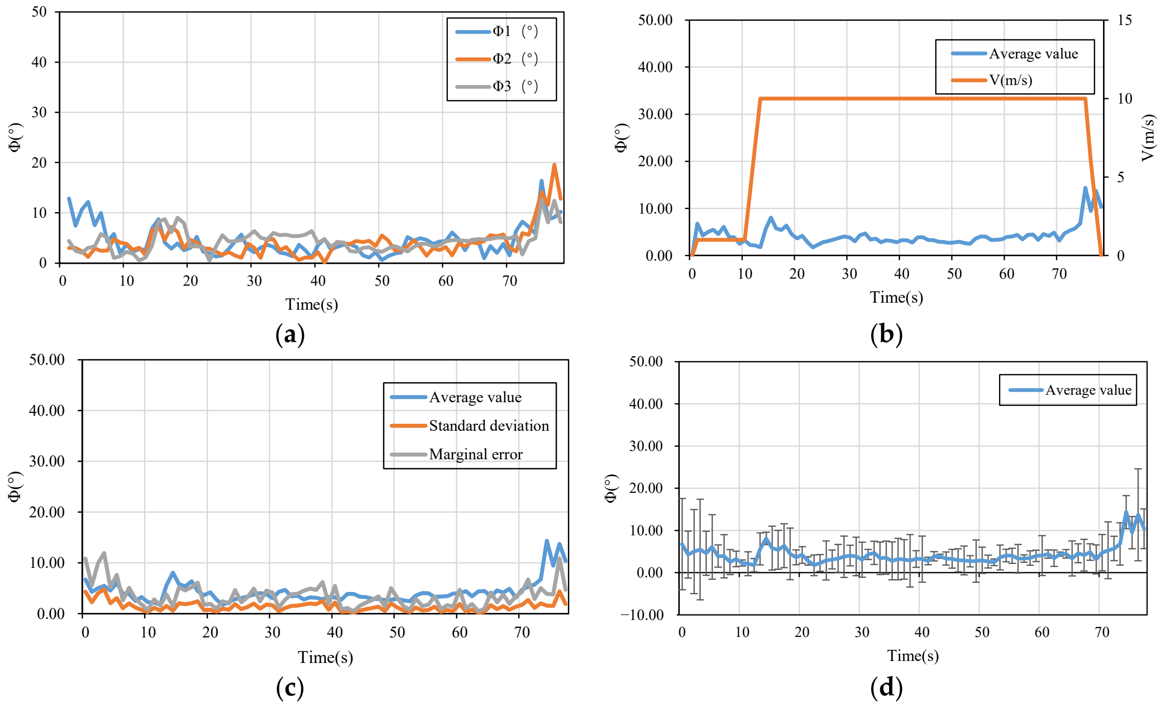

Figure 15. Swing Angle Response Curve of the UAV with a 30° Swing-Elimination Angle. (**a**) Variation curves of the swing angle for each flight trial. (**b**) Average swing angle-speed change curve. (**c**) Curves of the average value, standard deviation and marginal error of the swing angle. (**d**) Error bars of average swing angle.

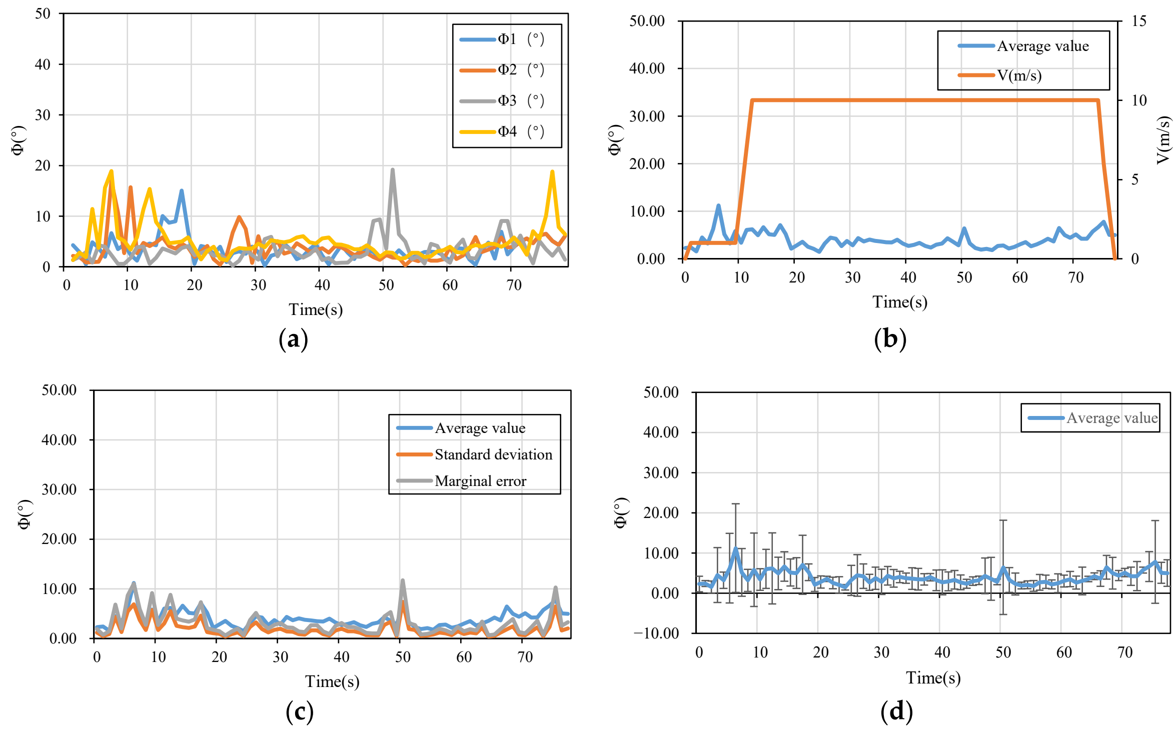

Figure 16. Swing Angle Response Curve of the UAV with a 50° Swing-Elimination Angle. (**a**) Variation curves of the swing angle for each flight trial. (**b**) Average swing angle-speed change curve. (**c**) Curves of the average value, standard deviation and marginal error of the swing angle. (**d**) Error bars of average swing angle.

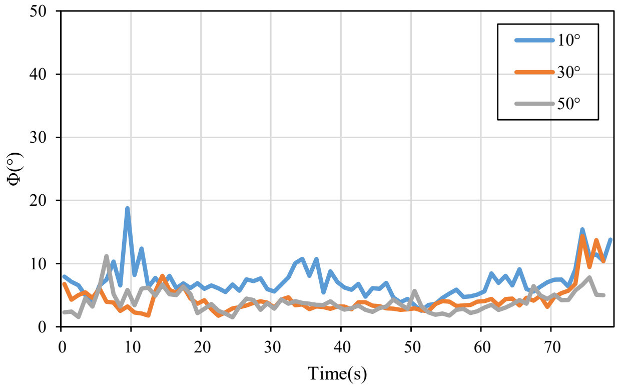

Figure 17. Swing angle state responses under different anti-swing parameters.

Analysis: From Equation (18), this equation describes the motion along the inertial x-axis. $(\boldsymbol{M}+\boldsymbol{m})\ddot{x}$ is the inertial force of the aircraft and the load as a whole. The terms on the right-hand side of the equation come from the traction effect of the load swing on the aircraft (the x-component of the rope tension). The swing-elimination angle is essentially the maximum allowable swing angle actively constrained by the flight control and the threshold of attitude compensation limitation. By restricting attitude deflection, adjusting acceleration input, and suppressing coupling torque, it intervenes in the excitation terms, gravity-restoring terms, and coupling terms in the equation, thereby regulating the swing amplitude. According to Equation (25), when the swing-elimination angle is small, the attitude adjustment range of the UAV is strictly limited. The flight control forcibly restricts attitude compensation to limit the swing angle, and cannot effectively counteract the inertial excitation torque brought by acceleration. The acceleration coupling torque cannot be released, the initial swing suppression ability is weak, and the swing angle is relatively large. When the swing angle is relatively large, appropriately increasing the swing-elimination angle to 30°, with a reasonable attitude compensation threshold, can counteract the inertial excitation (such as $\boldsymbol{mlC_xC_y}\ddot{x}, \boldsymbol{mlC_yS_xC_x}\ddot{z}$) through a small-amplitude attitude deflection without introducing additional attitude oscillations. At the same time, it optimizes the effect of the gravity-restoring term ($\boldsymbol{mlgS_yC_y}$), effectively weakens the excitation torque during the acceleration phase, and the swing angle reaches the minimum value. When the swing angle is not large, increasing the swing-elimination angle to 50° over-relaxes the attitude limitation, increases the attitude deflection of the UAV, intensifies the non-linear deviation of the trigonometric functions in the equation, significantly increases the coupling term ($\boldsymbol{2ml^2S_yC_y}\dot{\theta}_x\dot{\theta}_y$), enhances the system's non-linear coupling, and instead amplifies the swing during the acceleration phase, causing the swing angle to rise again.

Based on the performance curves of the swing suppression angle parameter observed in this experiment (30° is optimal, 10° gives insufficient suppression, 50° triggers oscillations). These curves intuitively show the robustness window of the error-based feedback controller (usually PID) in the flight control system when handling a non-linear system. The anti-swing angle function can essentially be understood as follows: When the flight control detects that the deviation between the body attitude and the desired attitude exceeds this angle threshold, a set of control laws dedicated to attitude recovery are triggered or enhanced. If the threshold is set too low, the controller over-reacts to small swings. It may trigger often or have low gain, so the suppression cannot match the swing energy. If the threshold is set too high, the system has "low-gain" or "no special compensation" at the start of a swing. It only intervenes strongly when the swing gets large. Such strong control under large errors is very likely to cause overshoot and continuous oscillation due to phase lag and system nonlinearity, that is, the so-called "over-correction". In control theory, this is directly related to the problems of gain scheduling and nonlinear control system design.

A core advantage of sliding-mode control and back-stepping control is their ability to offer consistent, stable performance across the full state range. This avoids performance decline due to incorrect threshold or gain settings [43]. The experiment in this paper reveals the limitations of the relatively simple control strategy adopted by commercial flight controls in the form of engineering parameters.

Based on the analysis of the experimental results, the adaptive parameter management procedure requires further development. A simple load-speed adaptive look-up table function can be developed in the flight control software. Based on the conclusions of this experiment, a two-dimensional parameter table can be preset. When the load gets heavier or the flight speed rises, the system can automatically adjust the anti-swing angle between 20 and 40 instance, it leans towards 35° in heavy-load and high-speed cases, and towards 25° in light-load and low-speed ones. For current industrial-grade logistics drones, it should be noted that the anti-swing angle optimization is only effective within the reactive control architecture of the current flight control. For swings from severe external disturbances or extreme maneuvers, the key is using feed-forward-feedback compound control or disturbance-observer-based control. This goes beyond parameter adjustment. Also, the optimal anti-swing angle can only improve the maximum swing in the deceleration stage, not get rid of it. This once again confirms that this parameter adjustment is a damage-control means rather than a fundamental solution. To break through this performance boundary, the control algorithm itself must be upgraded.

This section discussed the influence of different anti-swing angles on the swing angle of the suspended load. The UAV was operated with a 15 kg slung load, a trapezoidal velocity profile, and the normal flight mode. During the acceleration phase, affected by the acceleration excitation term and the non-linear coupling term, a 10° constraint is too strong and a 50° constraint is too weak, both of which will exacerbate the swing. A 30° swing-elimination angle can achieve a dynamic balance between excitation and constraint, resulting in the optimal swing angle. During the deceleration phase, without strong acceleration excitation, a large swing-elimination angle can fully utilize attitude compensation and gravity-restoring torque, and the swing angle continuously decreases as the swing-elimination angle increases. During the constant-speed phase, the acceleration excitation is zero, and the swing is dominated by the coupling non-linear term. Too small a swing-elimination angle (10°) is likely to cause high-frequency control oscillations, while increasing the swing-elimination angle (30° or 50°) can smooth the control output and suppress coupling disturbances, significantly improving the swing stability during the constant-speed flight. From the above analysis, when the suspended load is unstable during high-speed flight, appropriately increasing the swing-elimination angle can effectively improve the stability of the suspended load. However, the swing-elimination angle should not be too large. When the swing angle of the suspended load can already converge and stabilize, increasing the swing-elimination angle at this time will prevent the swing angle of the suspended load from converging quickly. Therefore, as the flight speed of the UAV increases, the swing angle also increases accordingly, and the swing-elimination angle should be appropriately increased at this time.

Based on the Euler-Lagrange suspension dynamics equation and combined with multiple comparative experiments, this chapter systematically analyzed the influence laws of the suspended load mass, flight mode, flight speed curve, and swing-elimination angle on the swing characteristics of the UAV's suspended load. The dynamics model shows that the inertial excitation torque generated by the UAV's acceleration and deceleration is the core factor inducing the load swing. The coupling term, gravity-restoring torque, and time-varying equivalent moment of inertia jointly determine the swing amplitude and convergence characteristics. The strong non-linearity caused by the increase in the swing angle will further amplify the system's uncertainty and error fluctuations. Regarding the suspended load mass, an increase in the load mass will increase the gravity-restoring torque, effectively suppressing the peak swing angle, but it will also increase the system's equivalent moment of inertia, resulting in an extended swing settling time, forming an inherent constraint between stability and rapid dynamic response. Comparing the suspended-load mode and the normal mode, the UAV generates a relatively large swing angle during the acceleration phase in the suspended-load mode, while in the normal mode, relatively large swing angles are generated during both the acceleration and deceleration phases. But under the same acceleration, the swing angle in the suspended-load mode is larger. It can be seen that improper operation during manual flight may generate a larger swing angle compared to the normal mode. In the flight motion state, the drastic acceleration changes during the take-off acceleration and deceleration phases will significantly excite the load swing. During the constant-speed flight phase, there is no acceleration excitation. The swing is mainly dominated by non-linear coupling terms and weak external disturbances, with relatively gentle changes. Under different swing-elimination angle conditions, during the take-off acceleration phase, the swing angle first decreases and then increases as the swing-elimination angle increases. A 30° swing-elimination angle can achieve a dynamic balance between control constraints and non-linear coupling, with the best swing-suppression effect. During the deceleration phase, as the swing-elimination angle increases, the attitude compensation margin increases, the residual swing is continuously suppressed, and the swing angle gradually decreases. At the same time, a too-small 10° swing-elimination angle will cause high-frequency control oscillations due to overly strict attitude constraints, leading to increased swing-angle fluctuations during the constant-speed phase. However, larger anti-swing angles of 30° and 50° can smooth the control output, weaken coupling disturbances, and significantly improve the suspension stability during the constant-speed flight. In summary, the suspended load weight, flight mode, acceleration excitation characteristics, and swing-elimination control threshold jointly affect the swing behavior of the suspension system through coupled dynamic terms. Reasonably matching the load mass, flight mode, flight acceleration-deceleration strategy, and swing-elimination angle parameters is the key to achieving stable and safe flight of the UAV's suspension.

In summary, the work of this chapter not only obtains the initial performance state of the industrial-grade logistics UAV suspension system under the existing technical conditions. More importantly, these quantitative laws based on real-world scenarios provide a direct basis for the selection of scientific operation strategies in different task scenarios. At the same time, they also point out the bottlenecks of the current technology and guide the follow-up theoretical research on high-performance adaptive control.

5. Discussion

In this paper, the load-carrying stability of the UAV is improved by adjusting its inherent properties. Compared with the sliding-mode controller designed based on theories such as passivity proposed earlier, this type of controller can achieve a smaller steady-state error (<0.5°) in simulations. However, its performance highly depends on an accurate dynamic model. In this study, while the swing angle can reach a near-1° steady-state error, this depends on the coupling between factors like the slung-load mode, slung-load weight, flight speed, and swing-elimination angle. Therefore, the performance baselines established in this study (such as a 2° steady-state error, non-convergence at 10 m/s, etc.) can serve as a "touchstone" for evaluating the actual improvement effect of such advanced controllers on real-world industrial platforms.

Compared with methods using precise modeling and controller design, for example, Zheng et al. achieved a 40% reduction in the swing-angle amplitude through UDE + TD robust control (uncertainty estimation + tracking differentiator) + air-resistance modeling with the SPAD term [44]; Zhu et al. achieved a 35% reduction in the swing-angle amplitude through adaptive control + disturbance observer (DOB), considering the Dryden wind field and time-varying load [45]; Dong et al. proposed a two-stage active disturbance rejection control (ADRC), introduced virtual position to suppress the swing angle, and included the lifting-stage control, achieving a 50% improvement in the swing-angle suppression efficiency, an increase in the disturbance-rejection bandwidth, and a smooth lifting process without large-amplitude swings [46]. In this paper, by increasing the load from 6 kg to 15 kg, a 23.05% reduction in the swing-angle amplitude was achieved; by changing the flight mode, a 13.99% reduction was achieved; by adopting a gentle speed curve, a 19.91% reduction was achieved; and by changing the swing-elimination angle, better swing-angle control was achieved. When the swing-elimination angle was increased from 10° to 30°, a 56.98% reduction in the swing-angle amplitude was achieved. In comparison, this study also achieved good swing-angle control effects through more implementable methods, and in some strategies, such as controlling the swing-elimination angle, even better swing-angle control effects were achieved.

Compared with existing theoretical modeling and simulation studies focusing on small quadrotor UAVs, the innovations of this study are mainly reflected in three aspects. First, by focusing on the real-world application scenarios of industrial-grade commercial UAVs, this study obtains the quantitative influence laws of key factors like payload weight and flight mode through outdoor field measurements. This fills the technical gap between small UAV research and industrial-grade applications. Secondly, an optimization strategy using existing UAV built-in functions is proposed. It does not need complex non-linear control algorithms or reinforcement learning models. This lowers the technical implementation threshold and better meets logistics enterprises' operational needs. Also, the coupling between speed changes and swing suppression is analyzed. It shows that the acceleration strategy controls swing amplitude and the deceleration phase affects convergence difficulty, guiding trajectory planning more accurately. Compared with advanced control algorithms like Bouhabza et al.'s P-SMC passivity-based sliding-mode controller [25] and geometric control method [31], the strategies in this study are less accurate in swing suppression but highly practical in engineering. They do not rely on precise system identification or complex on-board computing resources, and can be directly applied to ordinary logistics UAVs. Compared to traditional input-shaping control [47], the speed trajectory optimization strategy in this study better suits the actual flight characteristics of industrial-grade UAVs. It also offers measured data support for the engineering application of input-shaping technology.

Despite the valuable application achievements obtained in this study, there are still the following limitations: (1) Limitation in experimental platform: this study is only conducted based on the DJI FlyCart30 UAV. Differences in flight control algorithms and power system response characteristics among different brands of UAVs may lead to deviations in the optimization effects of flight modes and anti-swing angles. Future research should be extended to multi-brand and multi-model industrial-grade logistics UAVs to establish a general mapping model between payload weight, flight speed, and swing suppression parameters. (2) Simplified handling of environmental factors: the experiments are completed under calm weather conditions, without considering the influence of complex environmental factors such as wind disturbance and temperature changes. In actual logistics scenarios, the uncertainty of the low-altitude wind field is an important inducement for slung-load oscillation. Subsequent studies need to conduct wind tunnel experiments and outdoor wind field measurements to investigate the impact of different wind speeds and directions on swing characteristics, and optimize the dynamic adjustment strategy of the anti-swing angle. (3) Limitations of payload characteristics: the custom payload adopted in this study is a homogeneous rigid body, while actual logistics goods have diverse shapes and center-of-gravity distributions. Irregular payloads may induce complex dynamic behaviors such as non-planar oscillation. In the future, payload samples with different shapes and center-of-gravity offsets should be designed to explore the influence of payload characteristics on the swing suppression strategy and improve the generality of the strategy. (4) Control range of experimental variables: In this study, the slung load weights only cover 6 kg and 15 kg (low load and medium load), and the experimental verification under the full-load state of 30 kg has not been carried out. The swing angles are only set at 10°, 30° and 50°; the speed range is also limited to 0–10 m/s, and the swing characteristics at the maximum speed of the UAV have not been considered. The rope length is fixed at 5 m, and the influence of rope length on the swing has not been studied. Due to the small number of experimental groups mentioned above, the detailed coupling effects among various control factors have not been discovered. In the future, more experimental data for different load levels, different speeds, and more levels of anti-swing angles need to be added to improve the flight strategy under all working conditions. (5) Limitations of measurement resolution: Due to the limitations of experimental equipment, although the fundamental frequency is captured, higher-order harmonics may be omitted. In the future, sensors with a higher sampling rate can be adopted to obtain more complete dynamic information.

In summary, the flight operation guide in this study applies not only to logistics and distribution. It can also be extended to various industrial-level applications like building material transport, power inspection material delivery, and emergency rescue material airdrop. It has high practical engineering application value. In addition, with the large-scale development of the drone logistics industry, future research will combine visual sensing technology to monitor the load swing state in real-time. Through reinforcement learning algorithms, flight parameters will be dynamically optimized to achieve adaptive control of swing suppression. The experimental data and operation guide of this research can offer new concepts and a foundation for the further development of the drone flight control system. They can speed up the development of a specialized flight mode for logistics hoisting scenarios, further reduce the operation threshold, and boost the widespread use of industrial-level logistics drones.

6. Conclusions

Through systematic outdoor experiments on the DJI FlyCart30 industrial-grade commercial logistics UAV, this paper conducts an in-depth analysis of the impacts of slung-load weight, flight mode, speed trajectory, and anti-swing angle on the stability of the slung-load system, and proposes targeted flight strategies. The main conclusions are as follows.

(1) Trade-off relationship between load and swing

A heavier payload reduces the peak swing angle during speed changes but prolongs the settling time. The payload weight should be selected according to mission requirements: appropriately increase the load for swing amplitude-sensitive tasks, and appropriately reduce the load for settling time-sensitive tasks. Compared with the normal mode, manual flight in the load-carrying mode can better control the maximum swing angle and greatly improve the convergence effect. However, the efficiency of manual flight is lower than that of the normal mode. Therefore, when high flight stability is required, it is recommended to use manual flight control. When high transportation efficiency is required and the requirement for stability is not high, it is recommended to use the normal route mode.

(2) Selection of flight mode must match mission priorities

Manual control in the suspended-load mode can achieve fine control of the swing angle at the destination, making it suitable for tasks with high stability requirements.

Automatic flight in normal mode is more efficient, making it suitable for large-batch logistics distribution with lower stability requirements.

(3) Speed trajectory significantly affects swing suppression effectiveness

High-speed flight will enhance the force coupling of the slung load, leading to difficulty in converging the swing angle; it is recommended that the cruising speed of slung-load flight be controlled within 5 m/s. For high-speed flight, an S-shaped progressive acceleration strategy should be adopted, with sufficient settling time reserved.

(4) Optimal range of the anti-swing angle is around 30°

Appropriately increasing the anti-swing angle can improve slung-load stability, but an excessively large angle will result in failure to converge the swing angle; the anti-swing angle should be dynamically adjusted with the increase in flight speed to achieve a balance between swing suppression and convergence speed.

Author Contributions: Conceptualization, W.Z. and Q.B.; investigation, R.W.; data curation, R.W.; writing—original draft, W.Z.; writing—review & editing, P.J., Y.W. and Q.L.; visualization, Y.W. and Q.L. All authors have read and agreed to the published version of the manuscript.

Funding: This research received no external funding.

Data Availability Statement: Due to privacy restrictions, the datasets used in this study are not publicly available but may be obtained from the corresponding author upon reasonable request.

Conflicts of Interest: Author Rui Wang was employed by the company China Design Group (China). The remaining authors declare that the research was conducted in the absence of any commercial or financial relationships that could be construed as a potential conflict of interest.

References

1. Li, M. Beyond Conventional Drones: A Review of Unconventional Rotary-Wing UAV Design. *Drones* **2025**, *9*, 323. [CrossRef]
2. Qu, W.L.; Chen, Y. Improved YOLOv8n Algorithm for UAV Aerial Target Detection. *Mod. Electron. Tech.* **2026**, *49*, 77–85. [CrossRef]
3. Chen, W.B.; Fu, X.J.; Jiang, Z.W.; Wang, R.; Lu, B.Y. Precision Spraying System of Plant Protection UAV Based on Improved YOLOv7. *J. Chin. Agric. Mech.* **2026**, *47*, 167–173. [CrossRef]
4. Wu, G.W.; Li, G.L.; Li, S.S.; Luo, X.; Zhuang, M. CNN-Based Small Target Intelligent Recognition for UAV Inspection in Power Maintenance. *Electron. Des. Eng.* **2025**, *33*, 146–149+155. [CrossRef]
5. Bi, R.; Gan, S.; Yuan, X.P.; Li, R.B.; Gao, S. UAV Route Planning and 3D Modeling Analysis in Different Terrain Environments. *Bull. Surv. Mapp.* **2022**, *4*, 83–89+129. [CrossRef]
6. Zhao, X.; Li, Z. Multi-UAV Multi-Dimensional Decision Cooperative Regional Search Based on DMPC. *Mod. Inf. Technol.* **2023**, *7*, 15–20+25. [CrossRef]
7. Chen, G.; Song, G.M.; Hao, S.; Gu, Y.; Song, A.G. Modeling and Control of a Dual-Tilt Fully Actuated Hexacopter UAV. *Chin. J. Sci. Instrum.* **2021**, *42*, 254–262. [CrossRef]
8. Yang, Z.X.; Li, S.Y.; Wei, C.; Li, Z.; Zhu, B. Robust Control of Underactuated Three-Degree-of-Freedom Helicopter Based on Low-Order Disturbance Estimator. *Acta Aeronaut. ET Astronaut. Sin.* **2024**, *45*, 150–165. [CrossRef]
9. Wang, Y.; Ye, H.; Yang, X.F. Passivity-Based and Potential Field Method for Quadrotor Obstacle Avoidance and Position Control. *Acta Aeronaut. ET Astronaut. Sin.* **2023**, *44*, 225–235. [CrossRef]
10. Han, X.W.; Xian, B.; Yang, S. Adaptive Control Design for UAV Suspended Aerial Transportation System. *Control Theory Appl.* **2020**, *37*, 999–1006.
11. Sun, N.; Yang, T.; Fang, Y.; Wu, Y.; Chen, H. Transportation Control of Double-Pendulum Cranes with a Nonlinear Quasi-PID Scheme: Design and Experiments. *IEEE Trans. Syst. Man Cybern. Syst.* **2019**, *49*, 1408–1418. [CrossRef]
12. Zhang, L.L.; Bai, L.Z.; Liang, J.S.; Qin, Z.Y.; Zhao, Y.J. Intelligent PID Control Method for Quadrotor UAV with Serial Humanoid Intelligence. *Comput. Syst. Sci. Eng.* **2024**, *48*, 1557–1579. [CrossRef]
13. Peng, T.B. Modeling and Anti-Swing Control Research of Quadrotor UAV Slung-Load System. Master's Thesis, Shenyang Aerospace University, Shenyang, China, 2024. [CrossRef]
14. Xia, T.Q. Modeling and Control Design of Quadrotor UAV Transportation System with Rigid Suspended Payload. Master's Thesis, Tianjin University of Technology, Tianjin, China, 2024. [CrossRef]

15. Xue, C.H. Research on Anti-Swing Control of Quadrotor UAV Slung-Load System Under Wind Disturbance. Master's Thesis, Hubei University of Arts and Science, Xiangyang, China, 2025. [CrossRef]
16. Che, W.J. Research on Anti-Swing Control Strategy for Under Constrained UAV Slung-Load Flight System. Master's Thesis, Lanzhou Jiaotong University, Lanzhou, China, 2024. [CrossRef]
17. Klausen, K.; Fossen, T.I.; Johansen, T.A. Nonlinear Control with Swing Damping of a Multirotor UAV with Suspended Load. *J. Intell. Robot. Syst.* **2017**, *88*, 379–394. [CrossRef]
18. Wang, C.G.; Fan, B.; Niu, Z.X.; Yang, C.H. Positioning and Anti-Swing Control of Quadrotor UAV with Double Pendulum Load. *Comput. Simul.* **2023**, *40*, 34–40+73.
19. Zhu, Z.Y.; Gou, Y.P.; Zhang, L.S.; Chu, K.B.; Gong, C.Y. Design of Active Anti-Swing Control System for Quadrotor UAV Suspension. *Res. Explor. Lab.* **2025**, *44*, 37–41. [CrossRef]
20. Yang, S.; Xian, B. Energy-Based Nonlinear Adaptive Control Design for the Quadrotor UAV System with a Suspended Payload. *IEEE Trans. Ind. Electron.* **2020**, *67*, 2054–2064. [CrossRef]
21. Xian, B.; Wang, S.Z.; Yang, S. An Online Trajectory Planning Approach for a Quadrotor UAV with a Slung Payload. *IEEE Trans. Ind. Electron.* **2019**, *67*, 6669–6678. [CrossRef]
22. Liang, X.; Fang, Y.; Sun, N.; Lin, H. A Novel Energy-Coupling-Based Hierarchical Control Approach for Unmanned Quadrotor Transportation Systems. *IEEE/ASME Trans. Mechatron.* **2019**, *24*, 248–259. [CrossRef]
23. Jiao, H.L.; Guo, Y.Y.; Zhu, Z.W. Anti-Swing Control of UAV Suspended Flight Based on Acceleration Compensation. *J. Comput. Appl.* **2021**, *41*, 604–610.
24. Yaşkıran, B.; Öztürk, M.; Gökçe, B. Review of SMC and FOSMC Strategies for Rotary Wing UAVs. *Fractal Fract.* **2026**, *10*, 200. [CrossRef]
25. Bouhabza, K.; Guiatni, M.; Bouzid, Y.; Hamerlain, M. Energy-Efficient Passivity-Based Sliding Mode Controller for Small-Scale Quadrotor UAV for Trajectory Tracking. *Unmanned Syst.* **2025**, *13*, 837–859. [CrossRef]
26. Zhang, Z.; Zhang, H. Fractional-order sliding mode with active disturbance rejection control for UAVs. *Appl. Sci.* **2025**, *15*, 556. [CrossRef]
27. Al-Qahtani, F.M.; Aldhaifallah, M.; El Ferik, S.; Saif, A.-W.A. Robust FOSMC of a Quadrotor in the Presence of Parameter Uncertainty. *Drones* **2025**, *9*, 303. [CrossRef]
28. Yu, G.; Cabecinhas, D.; Cunha, R.; Silvestre, C. Nonlinear backstepping control of a quadrotor-slung load system. *IEEE/ASME Trans. Mechatron.* **2019**, *24*, 2304–2315. [CrossRef]
29. Borja-Jaimes, V.; García-Morales, J.; Escobar-Jiménez, R.F.; Guerrero-Ramírez, G.V.; Adam-Medina, M. A Backstepping Sliding Mode Control of a Quadrotor UAV Using a Super-Twisting Observer. *Appl. Sci.* **2025**, *15*, 10120. [CrossRef]
30. Wu, B.; Guo, Y.; Zheng, J.; Li, Z.; Gong, J.; Hui, N.; Han, X. Research on the Stability of UAV Attitude Under Hybrid Control Integrating Active Disturbance Rejection Control and Super-Twisting Sliding Mode Control. *Appl. Sci.* **2025**, *15*, 5124. [CrossRef]
31. Wang, J.; Yuan, X.; Zhu, B. Geometric Control for Trajectory-Tracking of a Quadrotor UAV with Suspended Load. *IET Control Theory Appl.* **2022**, *16*, 1271–1281. [CrossRef]
32. Zhu, W.; Guo, X.; Fang, Y.C.; Zhang, X.Y. A Path-Integral-Based Reinforcement Learning Algorithm for Path Following of an Autoassembly Mobile Robot. *IEEE Trans. Neural Netw. Learn. Syst.* **2020**, *31*, 4487–4499. [CrossRef] [PubMed]
33. Albaker, B.M. A Deep Reinforcement Learning-Based Adaptive Control Strategy for UAVs in Dynamic and Complex Environments. *AL-Iraqia J. Sci. Eng. Res.* **2025**, *4*, 77–88. [CrossRef]
34. Shi, H.; Wu, H.; Xu, C.; Zhu, J.; Hwang, M.; Hwang, K.S. Adaptive image-based visual servoing using reinforcement learning with fuzzy state coding. *IEEE Trans. Fuzzy Syst.* **2020**, *28*, 3244–3255. [CrossRef]
35. Shi, H.; Xu, M.; Hwang, K.S. A Fuzzy Adaptive Approach to Decoupled Visual Servoing for a Wheeled Mobile Robot. *IEEE Trans. Fuzzy Syst.* **2020**, *28*, 3229–3243. [CrossRef]
36. Lü, Z.Y. Modeling and Control of Multi-Rotor UAV System with Slung Load. Doctoral Dissertation, Dalian University of Technology, Dalian, China, 2021. [CrossRef]
37. Beard, R.W. Quadrotor dynamics and control. *Brigh. Young Univ.* **2008**, *19*, 46–56.
38. Arnold, V.I. *Mathematical Methods of Classical Mechanics*; Springer Science & Business Media: Berlin/Heidelberg, Germany, 2013.
39. Hao, T.S. *Theoretical Mechanics*; Higher Education Press: Beijing, China, 2003.
40. Zhou, W.; Li, Z.; Liu, W.; Gao, S. Research on Attitude Control of Coaxial UAV Against Wind Disturbance Based on Adaptive Backstepping Method. *Aerosp. Control* **2025**, *43*, 39–46. [CrossRef]
41. Liu, H.; Guo, Y.; Zhang, Y.; Jiang, B. Robust fault-tolerant control for quadrotor UAVs with parameter uncertainties and actuator faults. *Control Theory Technol.* **2024**, *22*, 581–595. [CrossRef]
42. He, X.; Chen, Q.; Hao, W. Distributed Control of UAV Formation Based on Passive Sliding Mode. *Acta Aeronaut. ET Astronaut. Sin.* **2026**, 1–12. Available online: https://link.cnki.net/urlid/11.1929.v.20251120.1507.020 (accessed on 13 February 2026). [CrossRef]
43. Xu, L.X.; Ma, H.J.; Guo, D.; Xie, A.H.; Song, D.L. Backstepping sliding-mode and cascade active disturbance rejection control for a quadrotor UAV. *IEEE/ASME Trans. Mechatron.* **2020**, *25*, 2743–2753. [CrossRef]

44. Zhu, Y.; Zheng, Z.; Shao, J.; Huang, H.; Zheng, W.X. Modeling, robust control design, and experimental verification for quadrotor carrying cable-suspended payload. *IEEE Trans. Autom. Sci. Eng.* **2024**, *22*, 6061–6075. [CrossRef]
45. Wang, R.; Shen, J.; Qiu, H.; Zhu, B. Adaptive control of quadrotor suspended load systems with variable payload and wind disturbances. *IET Control Theory Appl.* **2024**, *18*, 1686–1698. [CrossRef]
46. Zhao, K.; Zhang, J.; Shu, P.; Dong, X. Antiswing control strategy for quadrotor transporting a cable-suspended payload: A two-stage ADRC approach. *IEEE/ASME Trans. Mechatron.* **2024**, *30*, 2744–2755. [CrossRef]
47. Ma, W.J.; Guo, Y.Y. Vision-based Servo Anti-swing Control Method for Quadrotor Slung-load System. *J. Ordnance Equip. Eng.* **2024**, *45*, 268–277.